Supporting Information

Dendrite-Free Lithium Metal Batteries Achieved with Ce-MOF Membrane Coating with One-dimensional Continuous Oxygen-Containing Channel for Rapid Migration of Li ions

Chun-Lei Song,[a] Jun-Ran Luo,[a] Lin-Yuan Ma,[a] Ze-Hui Li,[a] Hongxia Wang, *[c], Yue-Peng Cai*[a] and Xu-Jia Hong*[b]

[a] School of Chemistry, South China Normal University, Guangzhou, 510006, P. R. China. E-mail: caiyp@scnu.edu.cn

[b] Guangzhou Municipal and Guangdong Provincial Key Laboratory of Molecular Target & Clinical Pharmacology, the NMPA and State Key Laboratory of Respiratory Disease, School of Pharmaceutical Sciences and the Fifth Affiliated Hospital, Guangzhou Medical University, Guangzhou 511436, China. E-mail: hongxujia@gzhmu.edu.cn

[c] School of Chemistry and Physics, Queensland University of Technology, Brisbane, Queensland 4001, Australia. E-mail: hx.wang@qut.edu.au

Table of Contents

the 1000th–1020 th (a), 1980 th–2000 th (b) and 3000 th–3020 th (c) hr.

Figure S18: The Li plating/stripping behavior at an areal capacity of 30 mA hr cm^{-2} with the current density of 15 mA cm^{-2} over 3,000 hr. The enlarged voltage profiles of the 405th–425 th (a), 505 th–525 th (b), 605 th–625 th (c) and 705 th–725 th (d) hr.

Figure S19: Voltage profiles of the symmetric cell with Ce-MOF-1 and bare Celgard separator at a current density of 0.5 mA cm^{-2} for 1 mAh cm^{-2}.

Figure S20: Photograph of the Li anode of the cell with different separators after cycling: (a)Ce-MOF-1, (b)Zr-MOF, (c) Ce-MOF-2, and (d) Ce-MOF-3.

Figure S21: The SEM photographs of the Li anode of the cell with different separator after cycling: (a)Ce-MOF-1, (b)Zr-MOF, (c) Ce-MOF-2, and (d) Ce-MOF-3.

Figure S22: The cross-section view of the Li anode of the cell with different separator after cycling: (a)Ce-MOF-1, (b)Zr-MOF, (c) Ce-MOF-2, and (d) Ce-MOF-3. The thickness of the loose lithium layer existing after the specific cycle were marked with red color.

Figure S23: SEM images of Li anodes with protection of the Zr-MOF disassembled from symmetric cells after (a) 10, (b) 50, and (c) 100 cycles at 5 mA cm^{-2} for 5 mAh cm^{-2}. SEM images of Li anodes with protection of the Ce-MOF-2 disassembled from symmetric cells after (d) 10, (e) 50, and (f) 100 cycles at 5 mA cm^{-2} for 5 mAh cm^{-2}. SEM images of Li anodes with protection of the Ce-MOF-3 disassembled from symmetric cells after (g) 10, (h) 50, and (i) 100 cycles at 5 mA cm^{-2} for 5 mAh cm^{-2}.

Figure S24: EIS spectra of Li anode of the symmetric cells with (a) Ce-MOF-1, (b)Zr-MOF, (c) Ce-MOF-2, and (d) Ce-MOF-3 after 20, 50 and 100 cycles at 5 mA cm^{-2} for 5 mAh cm^{-2}. (e) 3D scatter plot of EIS spectra of Li anode of the symmetric cells with different separators.

Figure S25: C 1s XPS spectra of Li anode of the symmetric cells with (a) Ce-MOF-1, (b)Zr-MOF, (c) Ce-MOF-2, and (d) Ce-MOF-3 after 100 cycles at 5 mA cm^{-2} for 5 mAh cm^{-2}. S 2p XPS spectra of Li anode of the symmetric cells with (e) Ce-MOF-1, (f)Zr-MOF, (g) Ce-MOF-2, and (h) Ce-MOF-3 after 100 cycles at 5 mA cm^{-2} for 5 mAh cm^{-2}.

Figure S26: F 1s XPS spectra of Li anode of the symmetric cells with (a) Ce-MOF-1, (b)Zr-MOF, (c) Ce-MOF-2, and (d) Ce-MOF-3 after 100 cycles at 5 mA cm^{-2} for 5 mAh cm^{-2}.

Figure S27: Li 1s XPS spectra of Li anode of the symmetric cells with (a) Ce-MOF-1, (b)Zr-MOF, (c) Ce-MOF-2, and (d) Ce-MOF-3 after 100 cycles at 5 mA cm^{-2} for 5 mAh cm^{-2}.

Figure S28: Ce 2p XPS spectra of Ce-MOF-1 after cycles.

Figure S29: In situ XRD of the symmetric cell with Ce-MOF-1.

Figure S30: (a) The coulomb efficiency of Li-Cu cell with different separators at an areal capacity of 1 mAh cm^{-2} with the current density of 1 mA cm^{-2}. (b) The coulomb efficiency of Li-Cu cell with Ce-MOF-1 at an areal capacity of 2 mAh cm^{-2} with the current density of 2 mA cm^{-2}. (c) The Voltage curve of the Li|Cu cells with different separators at first cycle. (d) The enlarged pictures of the Voltage curve of the Li|Cu cells with different separators at first cycle.

Figure S31: Voltage curves of the Li|Cu cells with different separators at different

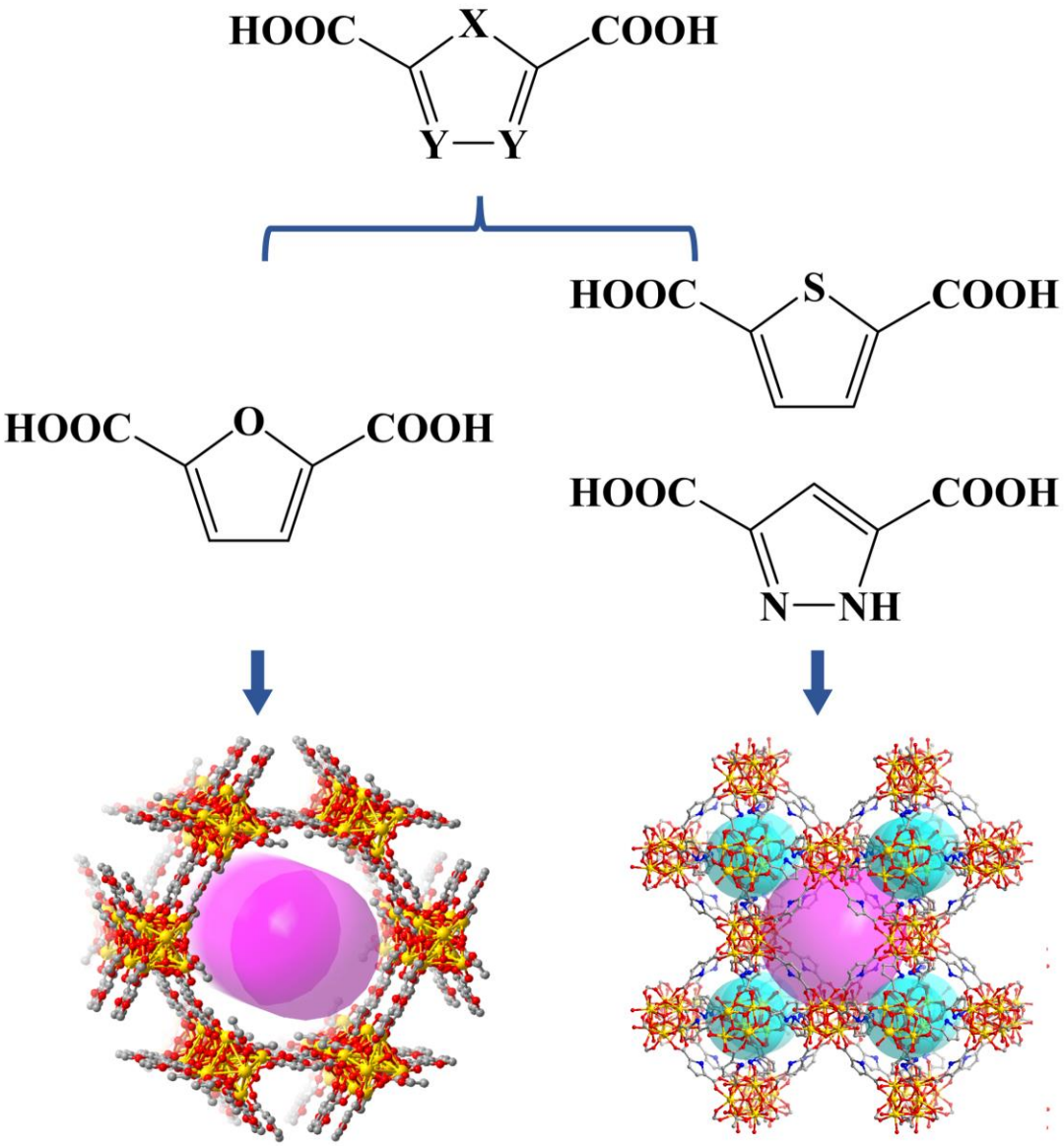

Figure S1. Different ligands correspond to the resulting structure of Ce-MOFs.

As shown in Figure **S1**, we synthesized a series of Ce-MOFs with different ligands. The frame channel of Ce-MOF synthesized from 2, 5-furan dicarboxylic acid is a continuous one-dimensional channel, which enables continuous running migration of Li^+. However, the frame channels of Ce-MOFs synthesized by 2, 5-thiophene dicarboxylic acid and 3, 5-pyrazole dicarboxylic acid are all cage channels, and Li^+ can only migrate by jumping. These three kinds of Ce-MOF were named as Ce-MOF-1, Ce-MOF-2 and Ce-MOF-3, respectively.

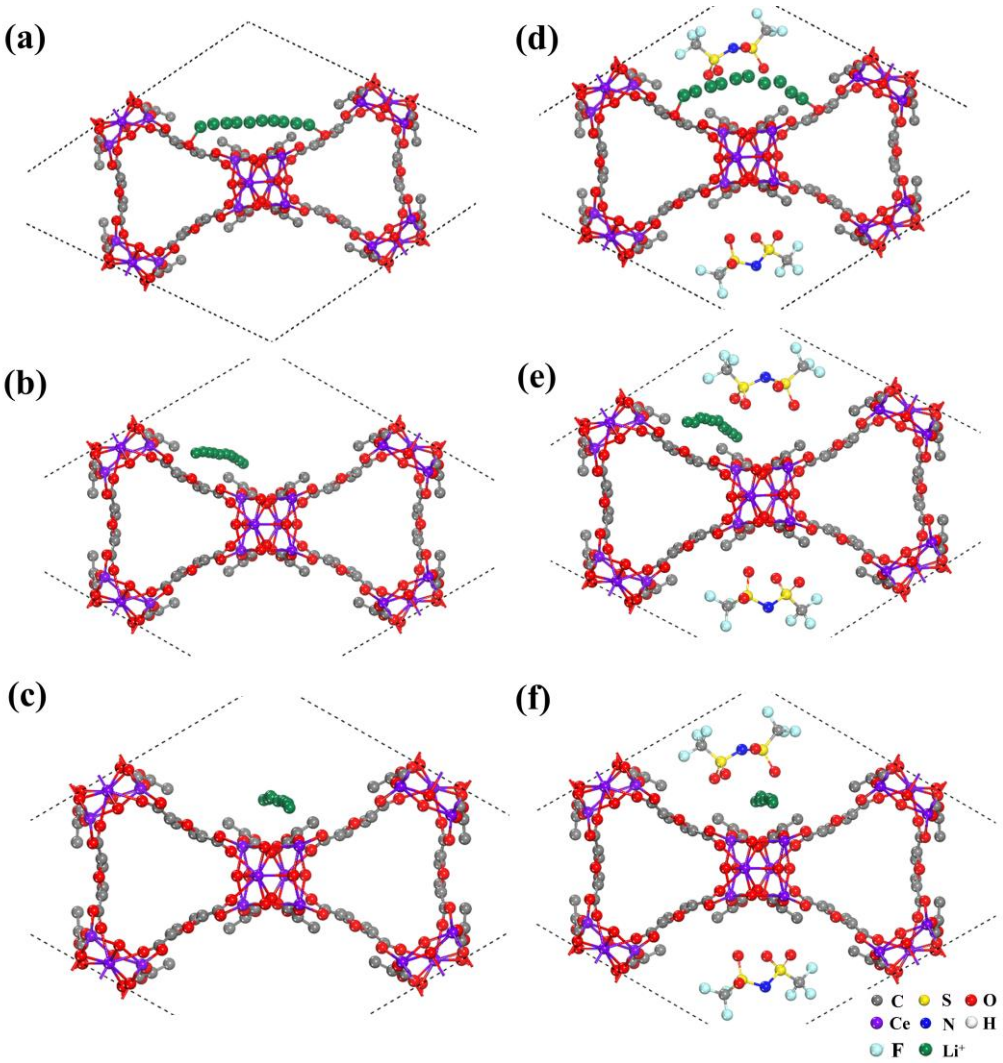

Figure S2. Li migration route in the Ce-MOF-1. Circular migration of Li^+ in the Ce-MOF-1 without LITFSI (a) or with LITFSI (d). Radial migration of Li^+ in the Ce-MOF-1 without LITFSI (b and c) or with LITFSI (e and f).

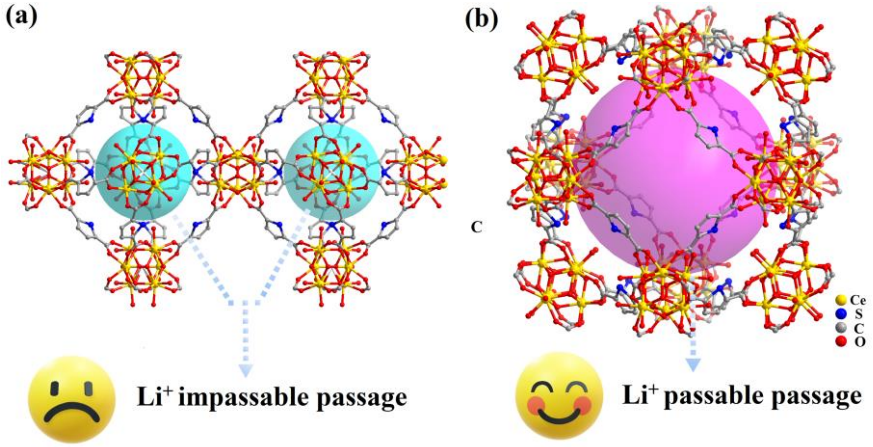

Figure S3. Interior channel structure of the Ce-MOF-2. (a) Li^+ impassable passage in the interior channel structure of Ce-MOF-2. (b) Li^+ passable passage in the interior channel structure of Ce-MOF-2.

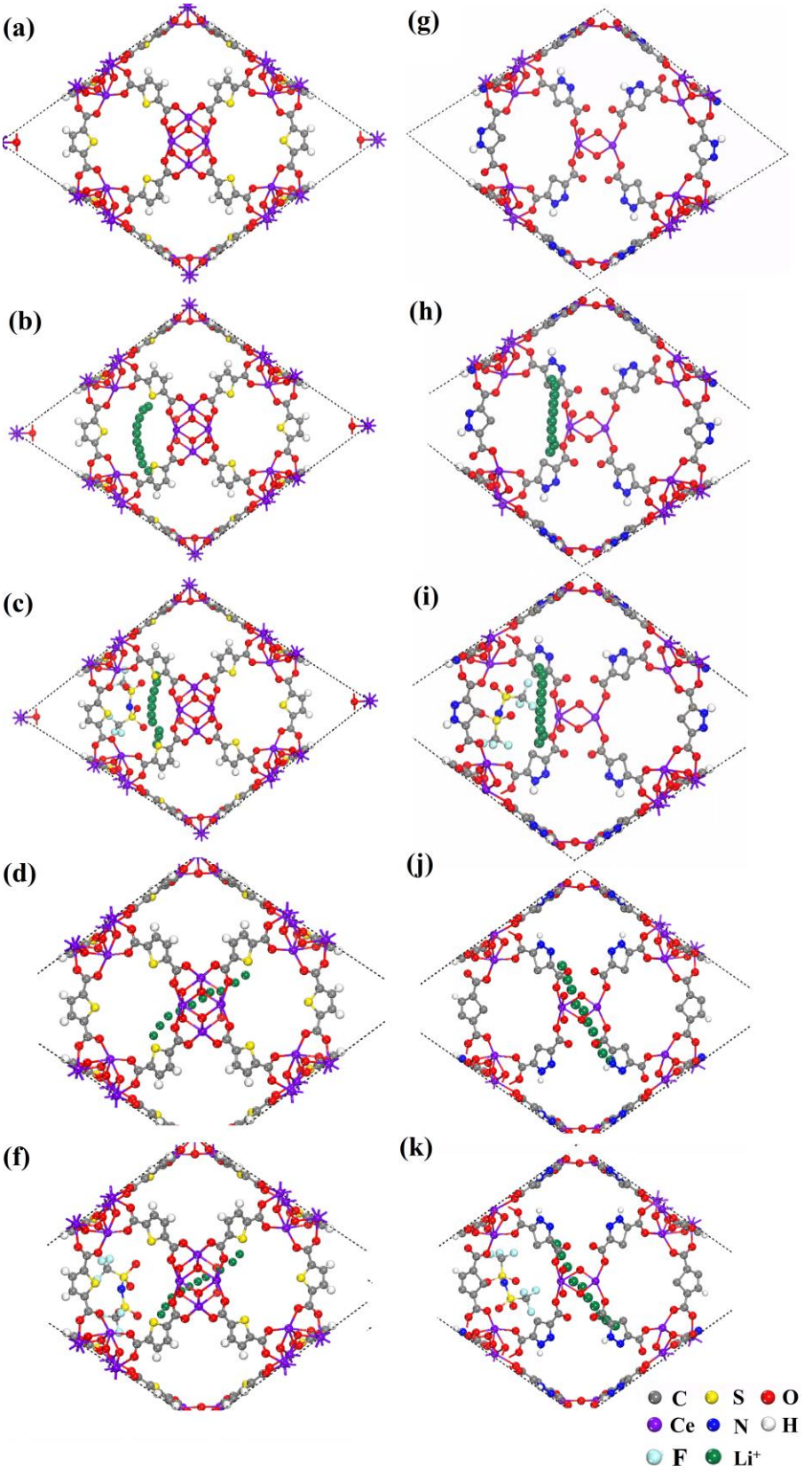

Figure S4. Structure of Ce-MOF-2 (a) and Ce-MOF-3 (g). Several different Li migration route in the Ce-MOF-2 without LITFSI (b and d) or with LITFSI (c and f). Several different Li migration route in the Ce-MOF-3 without LITFSI (h and j) or with LITFSI (i and k).

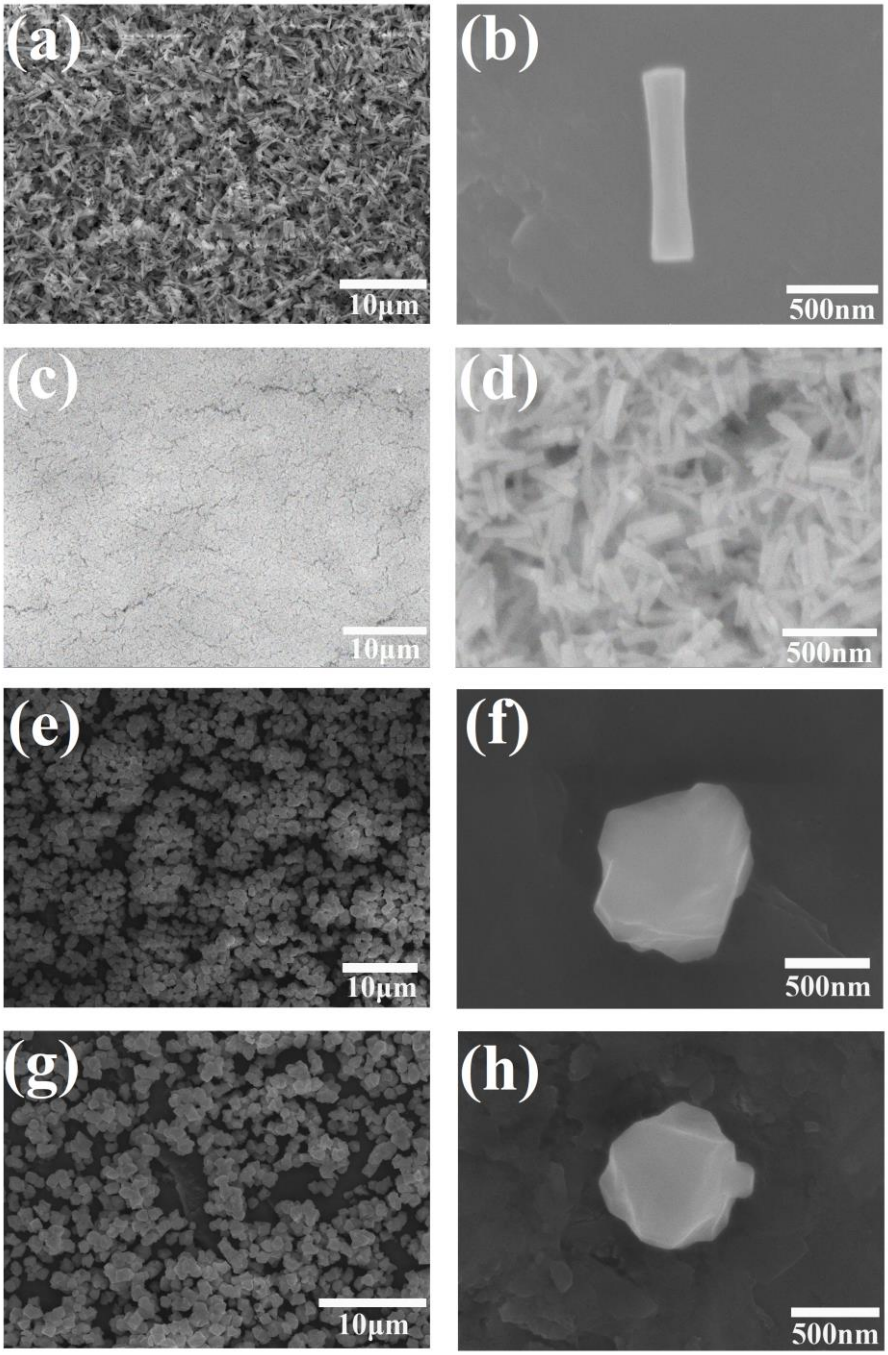

Figure S5.SEM images of (a, b) Ce-MOF-1, (c, d) Zr-MOF, (e, f) Ce-MOF-2, and (g, h) Ce-MOF-3.

As shown in Figure **S 5a** and **b**, the SEM image show that the Ce-MOF-1 was an extremely uniform rod with a size of approximately 1 μm. The SEM images of Zr-MOF were shown in the Figure **S 5c** and **d**, it can be clearly seen that the Zr-MOF also presents uniform rod shape, but it is much smaller than that of Ce-MOF-1. Moreover, the SEM images show uniform and irregular particles with the size of about 1 μm of Ce-MOF-2 and Ce-MOF-3 (Figure **S 5e**-**h**).

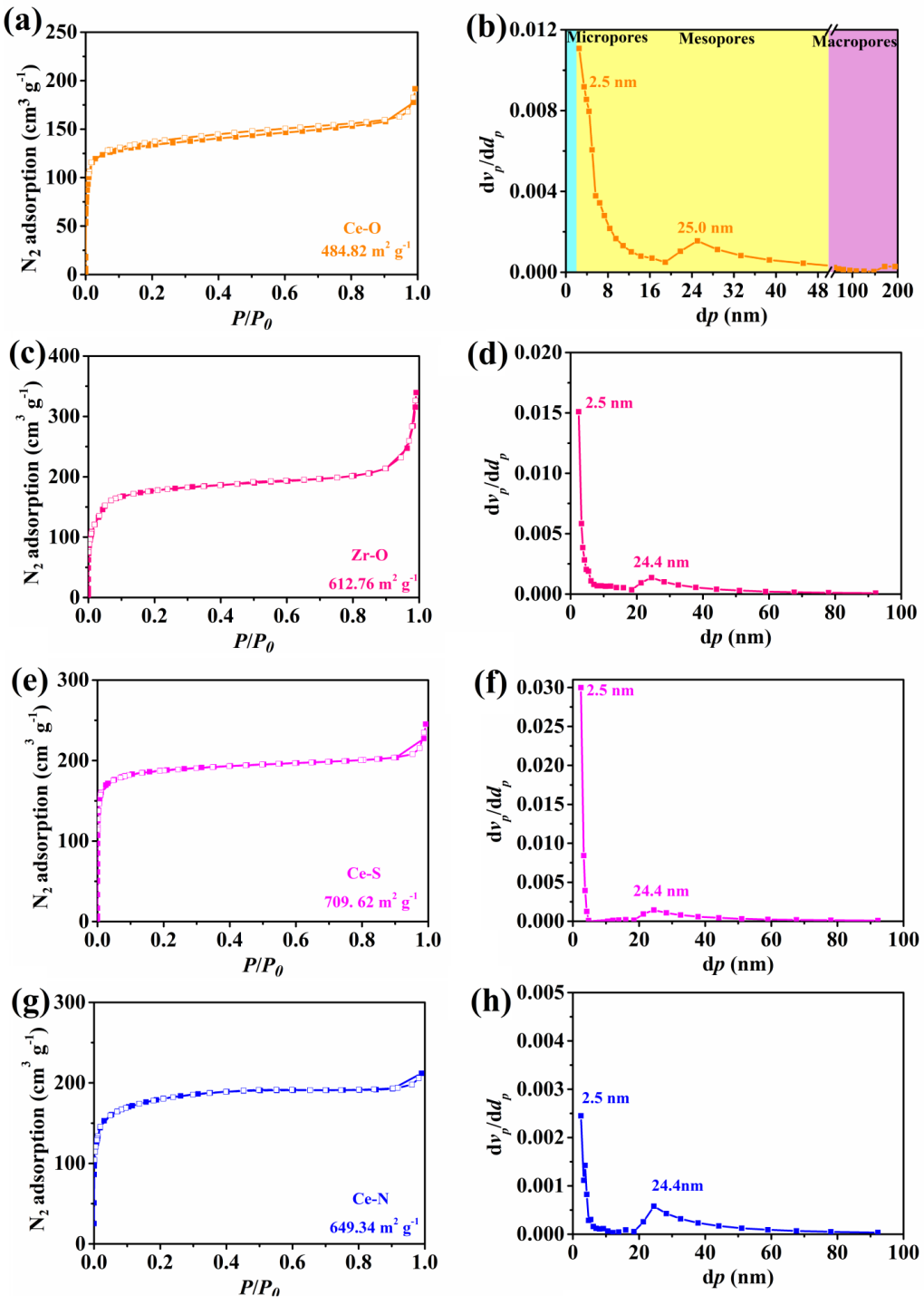

Figure S6. (a) N_2 adsorption–desorption isotherm and (b) pore size distribution of Ce-MOF-1. (c) N_2 adsorption–desorption isotherm and (d) pore size distribution of Zr-MOF. (e) N_2 adsorption–desorption isotherm and (f) pore size distribution of Ce-MOF-2. (g) N_2 adsorption–desorption isotherm and (h) pore size distribution of Ce-MOF-3.

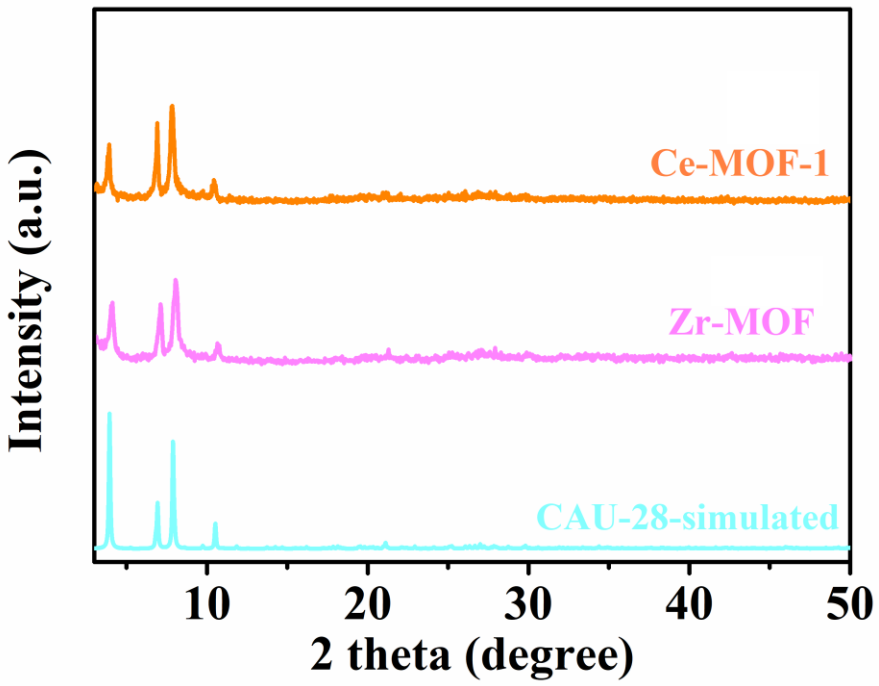

Figure S7. XRD patterns of Ce-MOF-1, Zr-MOF.

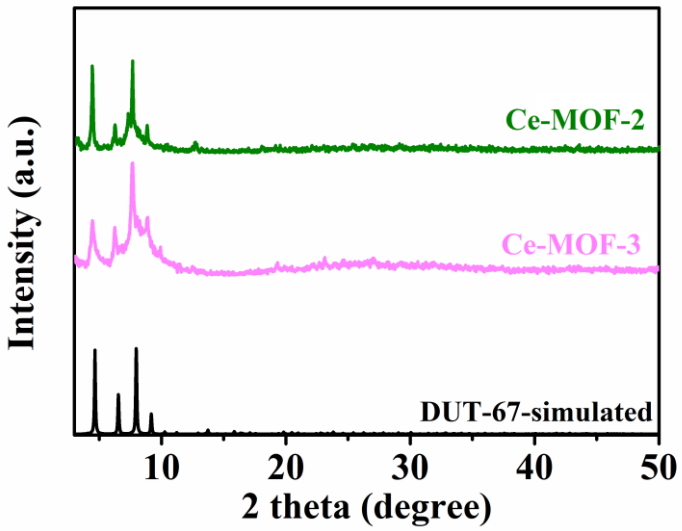

Figure S8. XRD patterns of Ce-MOF-2, Ce-MOF-3.

As shown in Figure **S7** and **S8**, the XRD patterns shows that Ce-MOF-1 and Zr-MOF were CAU-28-MOF, and Ce-MOF-2 and Ce-MOF-3 were DUT-67-MOF.

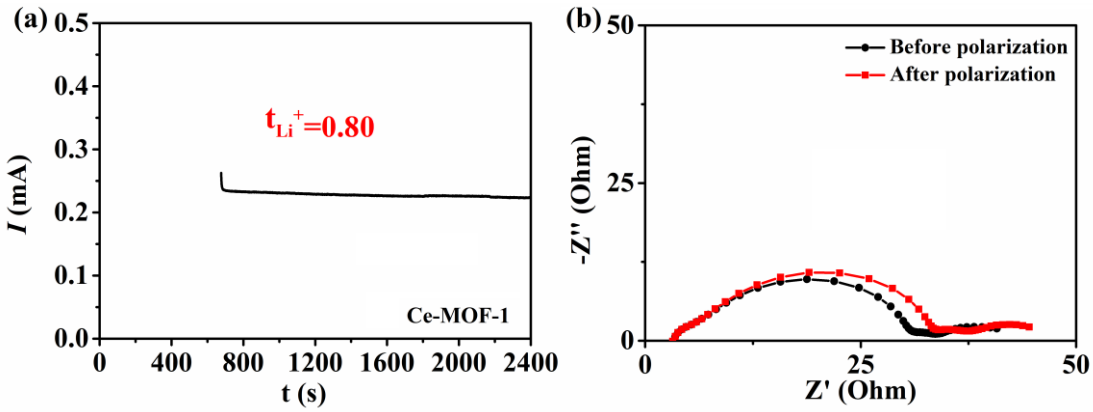

Figure S9. (a) Impedance spectra of the Li||Ce-MOF-1||Li cell before and after the dc polarization. (b) Li||Ce-MOF-1||Li cell after a perturbation of 10 mV direct current pulse.

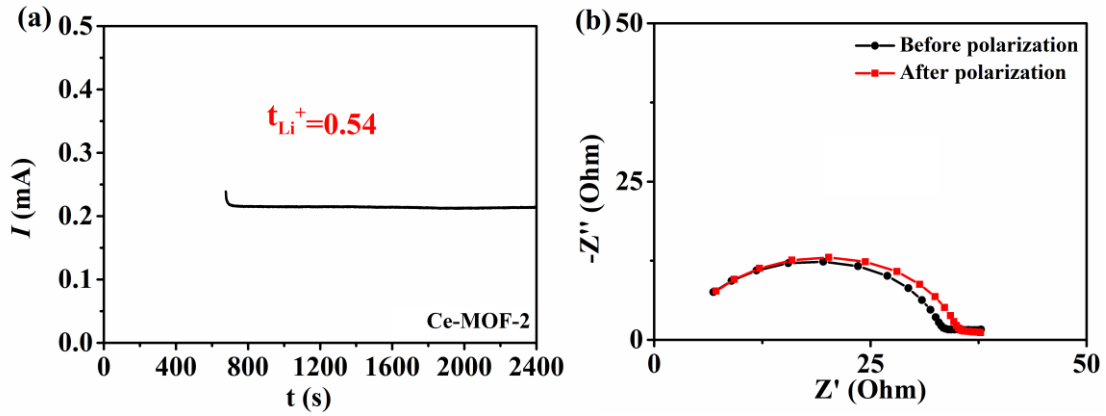

Figure S10. (a) Impedance spectra of the Li||Zr-MOF||Li cell before and after the dc polarization. (b) Li||Zr-MOF||Li cell after a perturbation of 10 mV direct current pulse.

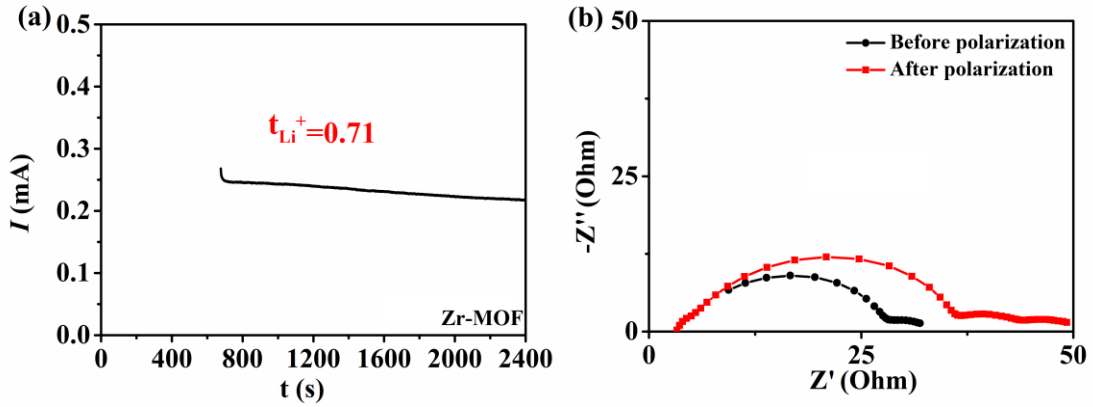

Figure S11. (a) Impedance spectra of the Li||Ce-MOF-2||Li cell before and after the dc polarization. (b) Li||Ce-MOF-2||Li cell after a perturbation of 10 mV direct current pulse.

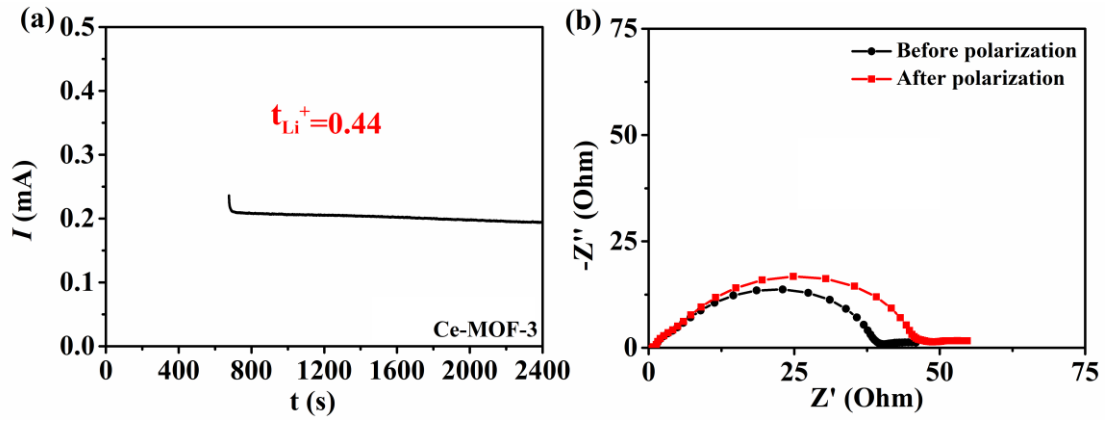

Figure S12. (a) Impedance spectra of the Li||Ce-MOF-3||Li cell before and after the dc polarization. (b) Li||Ce-MOF-3||Li cell after a perturbation of 10 mV direct current pulse.

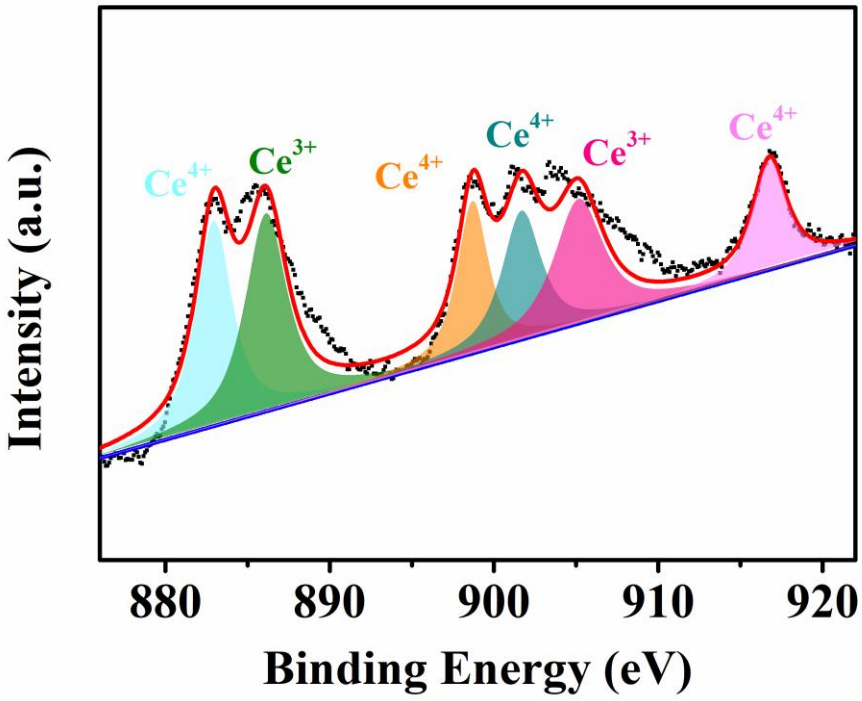

Figure S13. XPS Ce spectra of Ce-MOF-1.

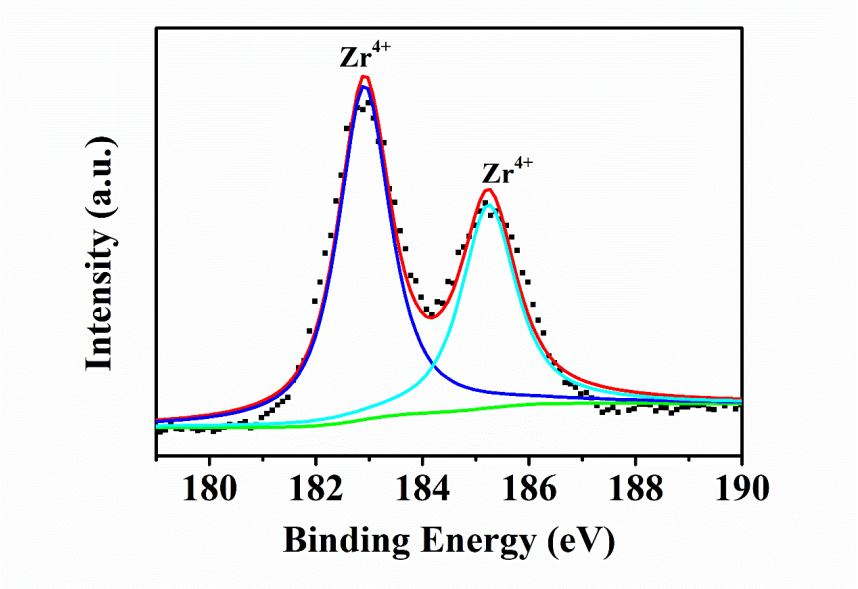

Figure S14. XPS Zr spectra of Zr-MOF.

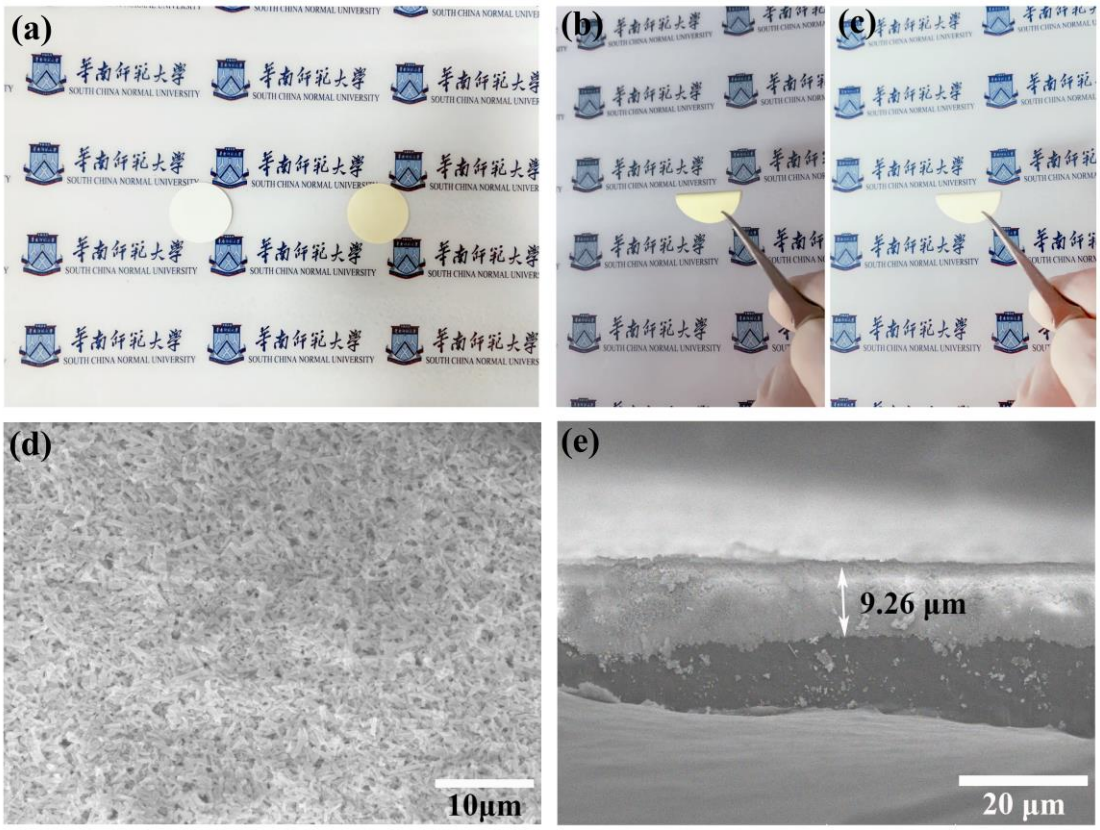

Figure S15. (a, b, c) The photograph of the Ce-MOF-1 coated separator. (d) The SEM image of the Ce-MOF-1 coated separator. (e) The cross-section view of the Ce-MOF-1 coated separator.

As shown in Figure **S15**, SEM tests show that Ce-MOF-1 was evenly distributed on the separator with the thickness of only ~9.26 μm， while the weight of coating materials is just ~0.11 mg cm^{-2}, which will not have much impact on the overall energy density of the battery.

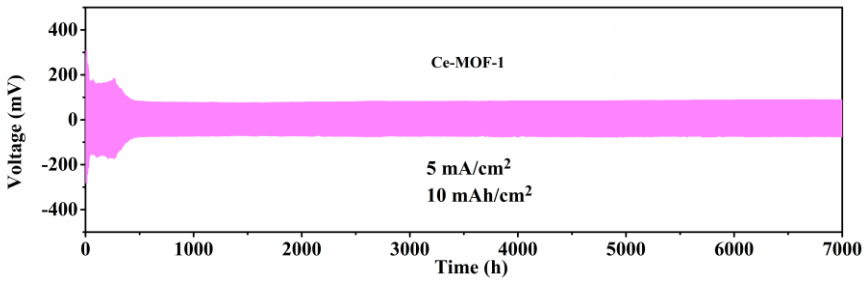

Figure S16. Voltage profiles of the symmetric cell with Ce-MOF-1 at a current density of 5 mA cm^{-2} for 10 mAh cm^{-2}.

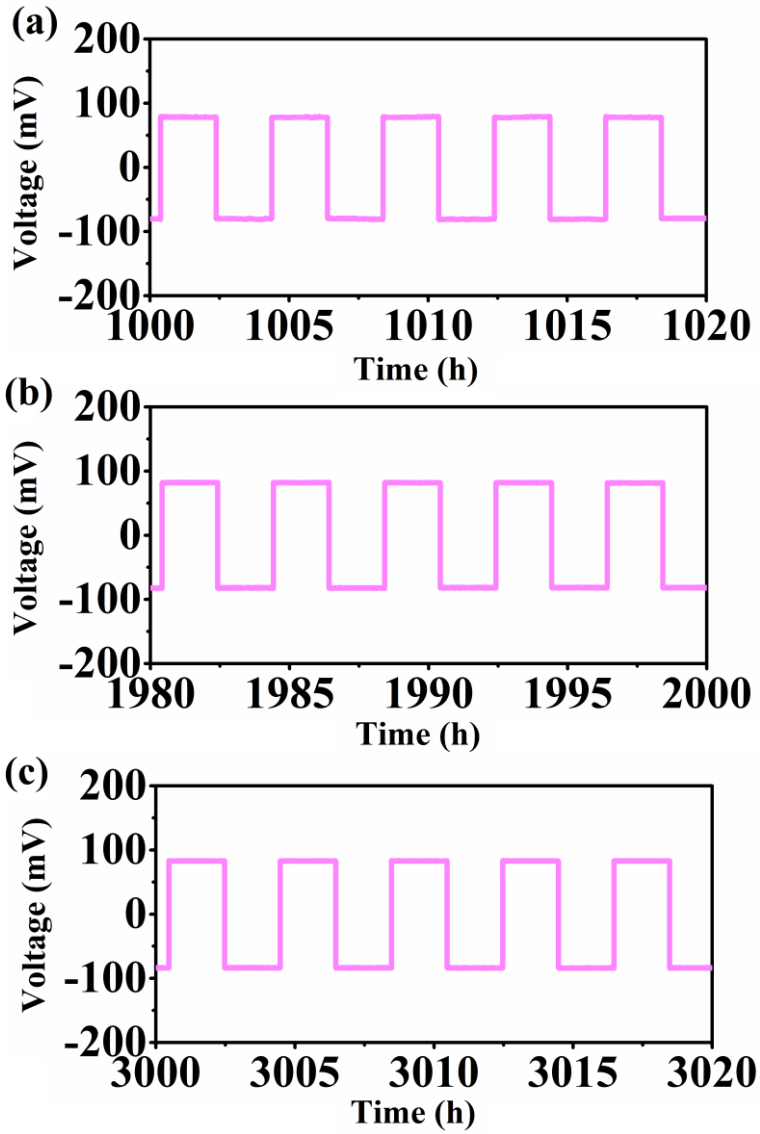

Figure S17. The Li plating/stripping behavior at an areal capacity of 30 mA hr cm^{-2} with the current density of 15 mA cm^{-2} over 3,000 hr. The enlarged voltage profiles of the 1000th–1020th (a), 1980th–2000th (b) and 3000th–3020th (c) hr.

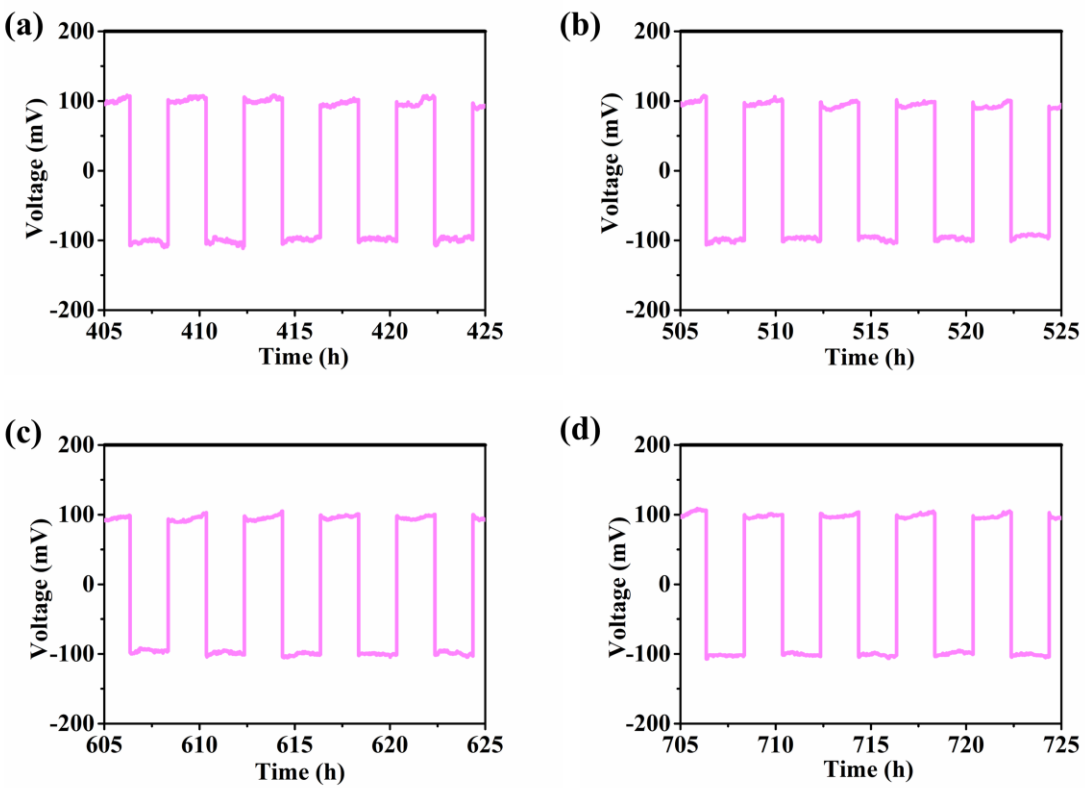

Figure S18. The Li plating/stripping behavior at an areal capacity of 30 mA hr cm^{-2} with the current density of 15 mA cm^{-2} over 3,000 hr. The enlarged voltage profiles of the 405th–425 th (a), 505 th–525 th (b) , 605 th–625 th (c) and 705 th–725 th (d) hr.

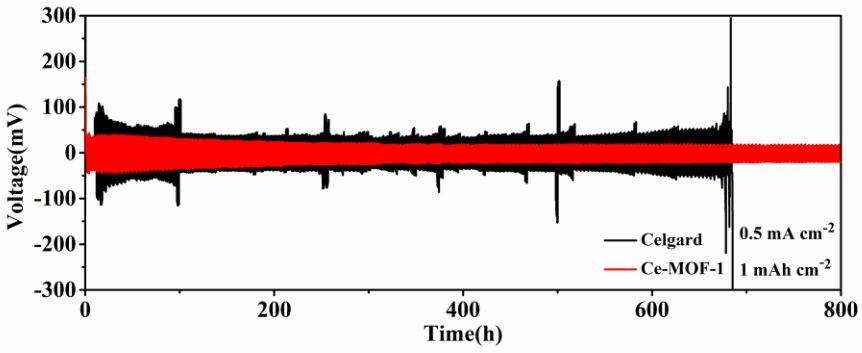

Figure S19. Voltage profiles of the symmetric cell with Ce-MOF-1 and bare Celgard separator at a current density of 0.5 mA cm^{-2} for 1 mAh cm^{-2}.

As shown in Figure **S19**, at 0.5 mA cm^{-2} and 1 mAh cm^{-2}, the voltage hysteresis of the symmetrical cell with Celgard started to increase very early. This is probably due to the continuous consumption of electrolyte and the growth of lithium dendrites. In contrast, the cell based on Ce-MOF-1 showed a lower voltage hysteresis of 25 mV.

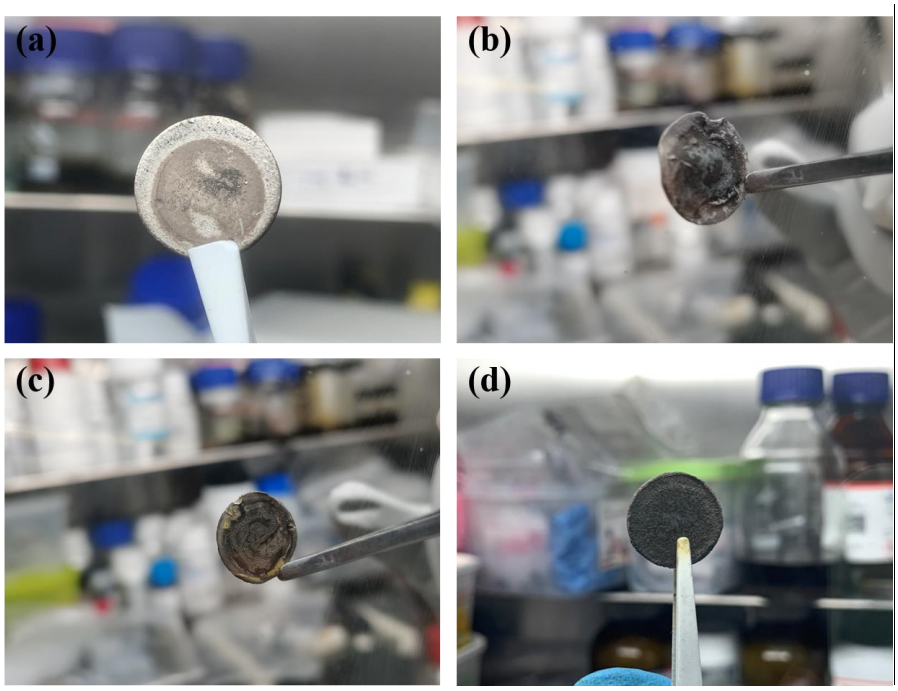

Figure S20. Photograph of the Li anode of the cell with different separators after cycling: (a)Ce-MOF-1, (b)Zr-MOF, (c) Ce-MOF-2, and (d) Ce-MOF-3.

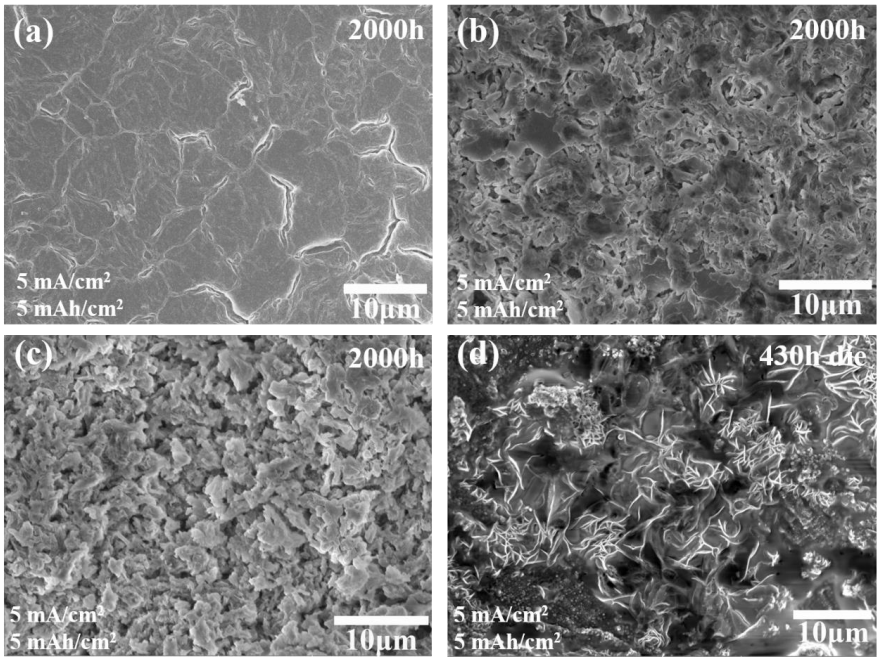

Figure S21. The SEM photographs of the Li anode of the cell with different separator after cycling: (a)Ce-MOF-1, (b)Zr-MOF, (c) Ce-MOF-2, and (d) Ce-MOF-3.

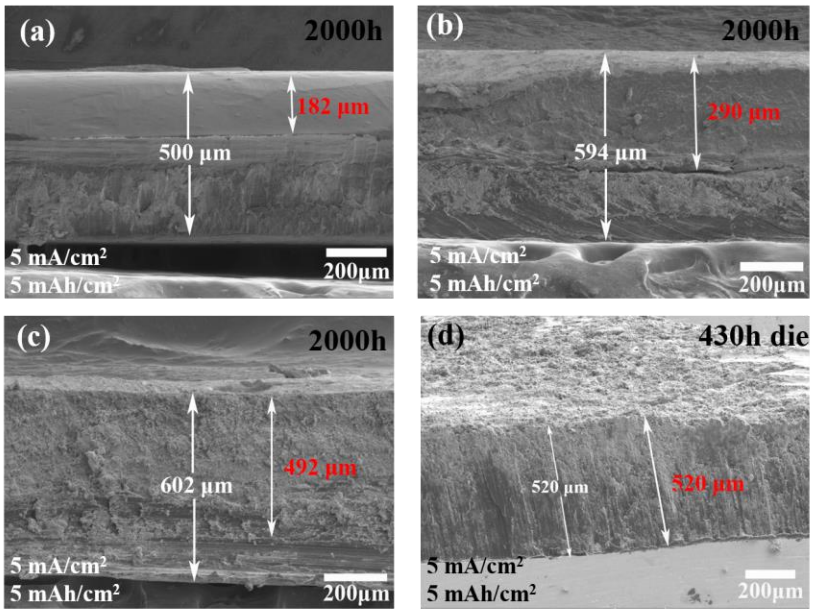

Figure S22. The cross-section view of the Li anode of the cell with different separator after cycling: (a)Ce-MOF-1, (b)Zr-MOF, (c) Ce-MOF-2, and (d) Ce-MOF-3. The thickness of the loose lithium layer existing after the specific cycle were marked with red color.

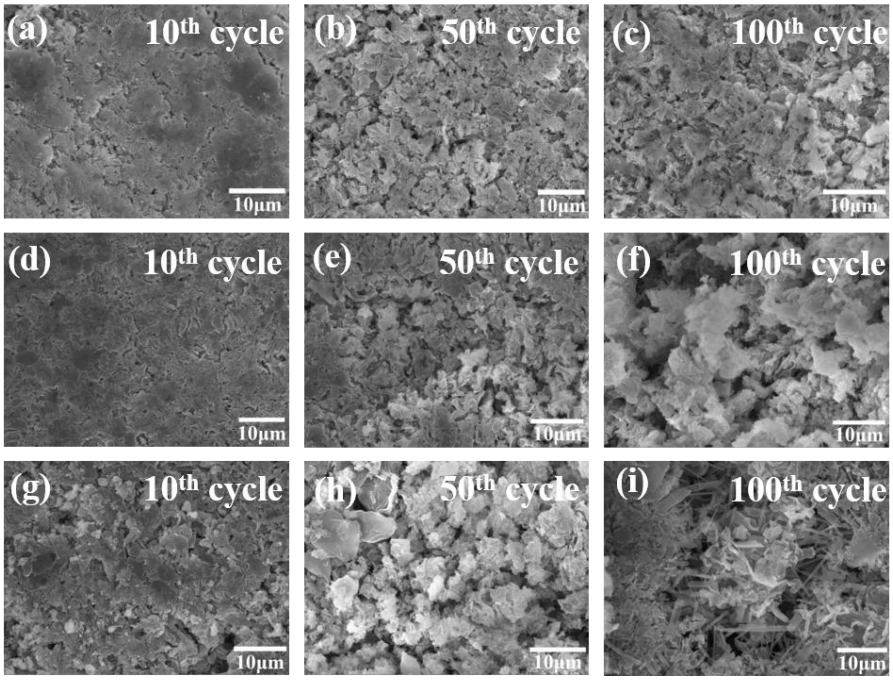

Figure S23. SEM images of Li anodes with protection of the Zr-MOF disassembled from symmetric cells after (a) 10, (b) 50, and (c) 100 cycles at 5 mA cm^{-2} for 5 mAh cm^{-2}. SEM images of Li anodes with protection of the Ce-MOF-2 disassembled from symmetric cells after (d) 10, (e) 50, and (f) 100 cycles at 5 mA cm^{-2} for 5 mAh cm^{-2}. SEM images of Li anodes with protection of the Ce-MOF-3 disassembled from symmetric cells after (g) 10, (h) 50, and (i) 100 cycles at 5 mA cm^{-2} for 5 mAh cm^{-2}.

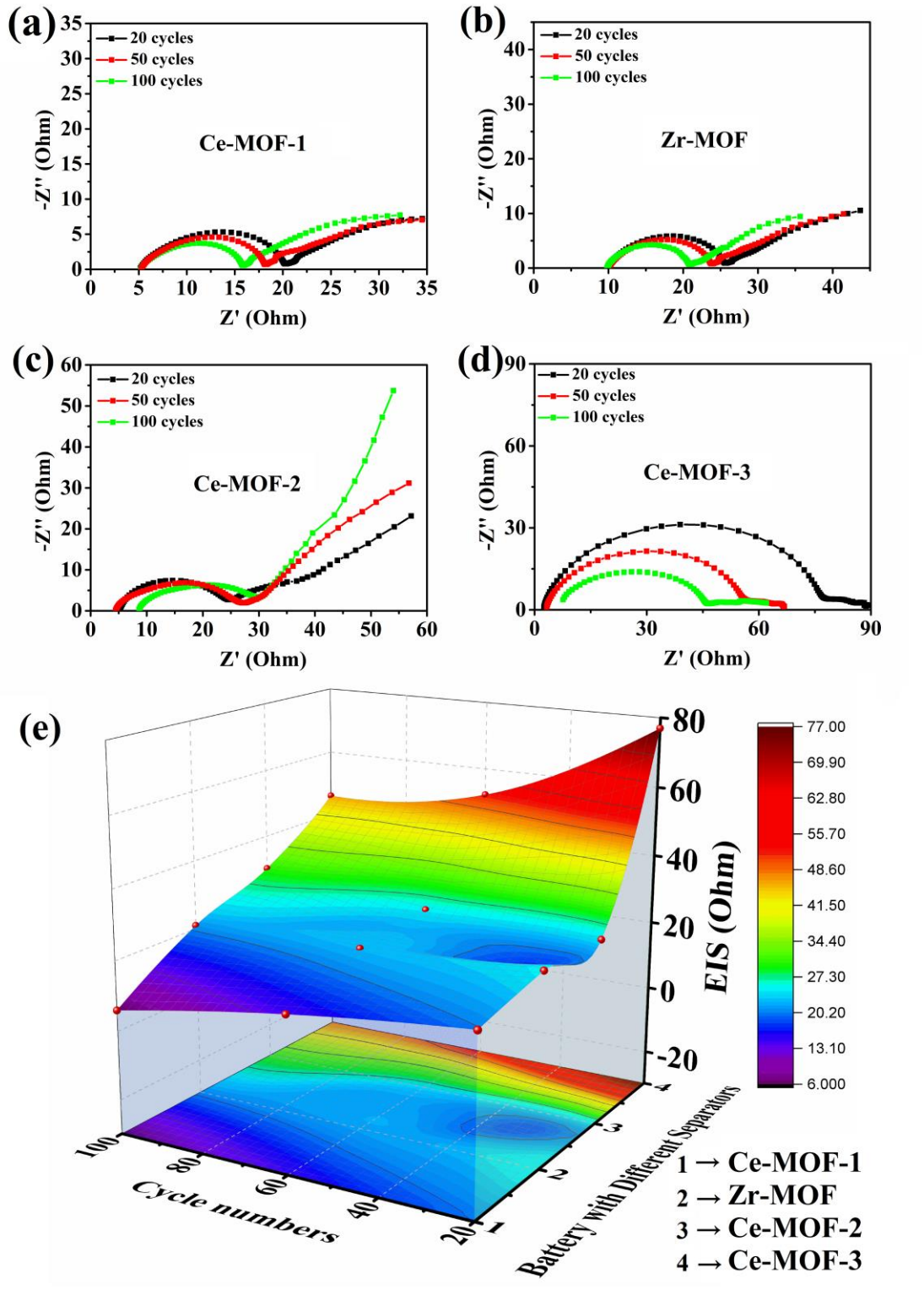

Figure S24. EIS spectra of Li anode of the symmetric cells with (a) Ce-MOF-1, (b)Zr-MOF, (c) Ce-MOF-2, and (d) Ce-MOF-3 after 20, 50 and 100 cycles at 5 mA cm^{-2} for 5 mAh cm^{-2}. (e)3D scatter plot of EIS spectra of Li anode of the symmetric cells with different separators.

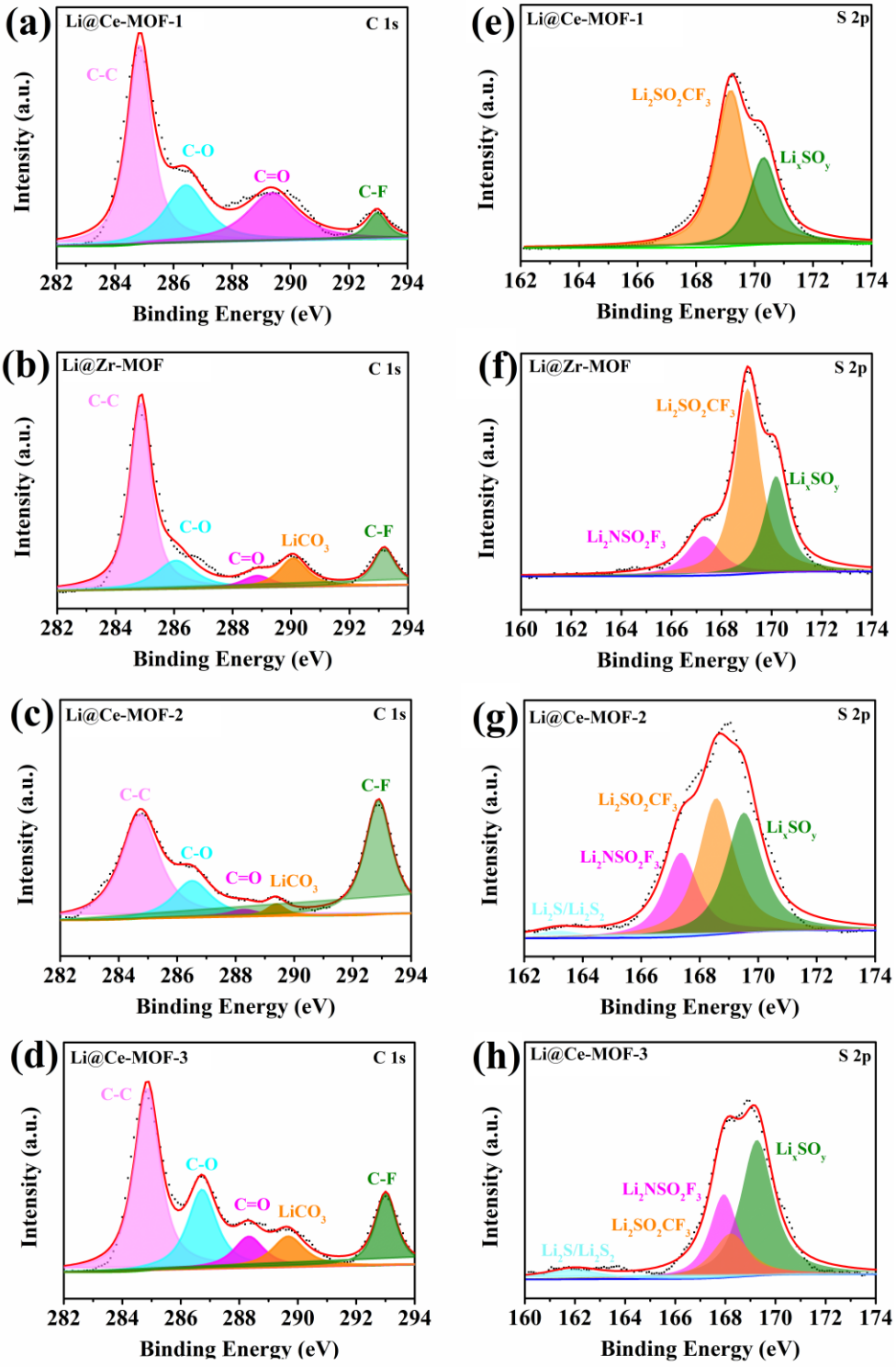

Figure S25. C 1s XPS spectra of Li anode of the symmetric cells with (a) Ce-MOF-1, (b)Zr-MOF, (c) Ce-MOF-2, and (d) Ce-MOF-3 after 100 cycles at 5 mA cm^{-2} for 5 mAh cm^{-2}. S 2p XPS spectra of Li anode of the symmetric cells with (e) Ce-MOF-1, (f) Zr-MOF, (g) Ce-MOF-2, and (h) Ce-MOF-3 after 100 cycles at 5 mA cm^{-2} for 5 mAh cm^{-2}.

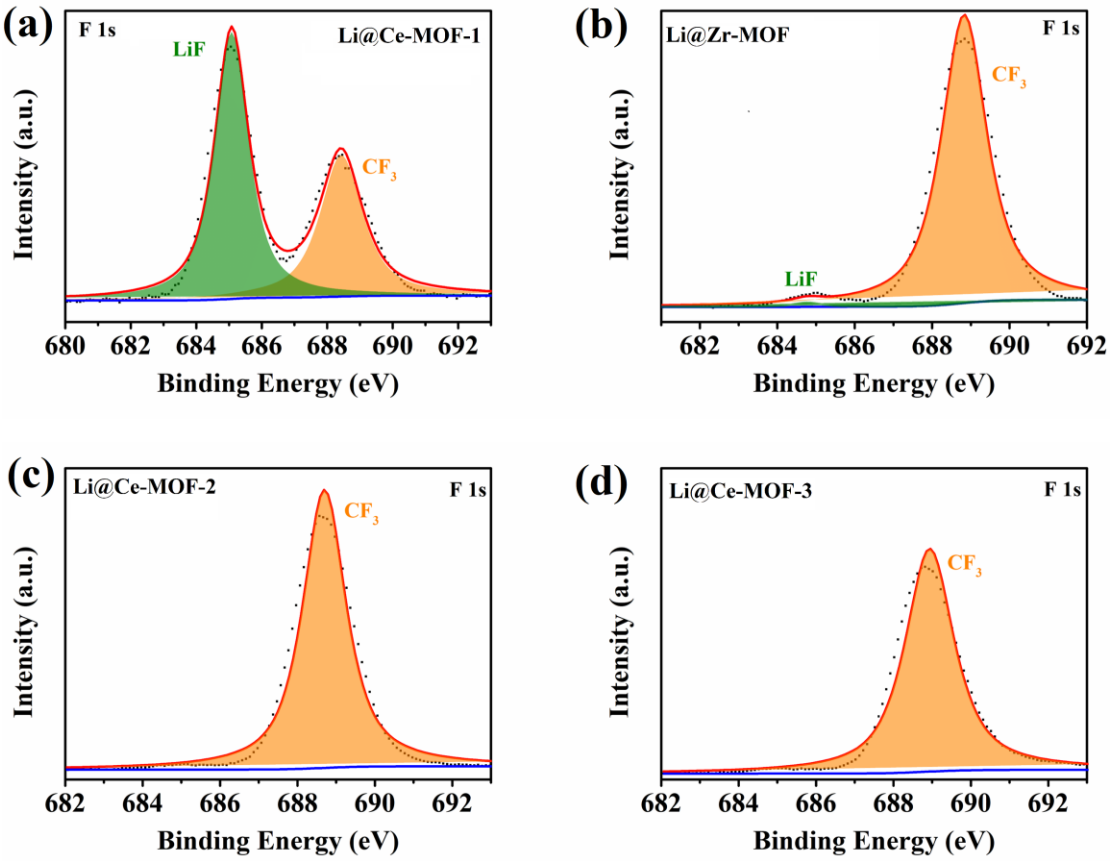

Figure S26. F 1s XPS spectra of Li anode of the symmetric cells with (a) Ce-MOF-1, (b)Zr-MOF, (c) Ce-MOF-2, and (d) Ce-MOF-3 after 100 cycles at 5 mA cm^{-2} for 5 mAh cm^{-2}.

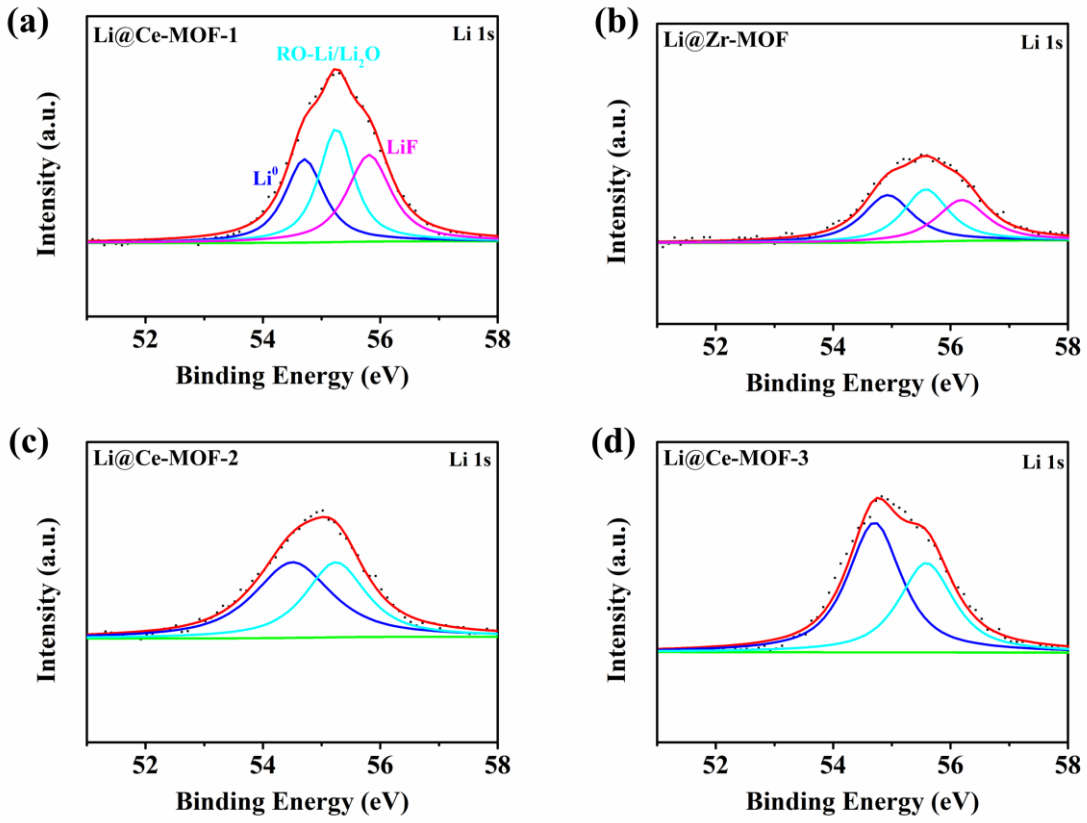

Figure S27. Li 1s XPS spectra of Li anode of the symmetric cells with (a) Ce-MOF-1, (b)Zr-MOF, (c) Ce-MOF-2, and (d) Ce-MOF-3 after 100 cycles at 5 mA cm^{-2} for 5 mAh cm^{-2}.

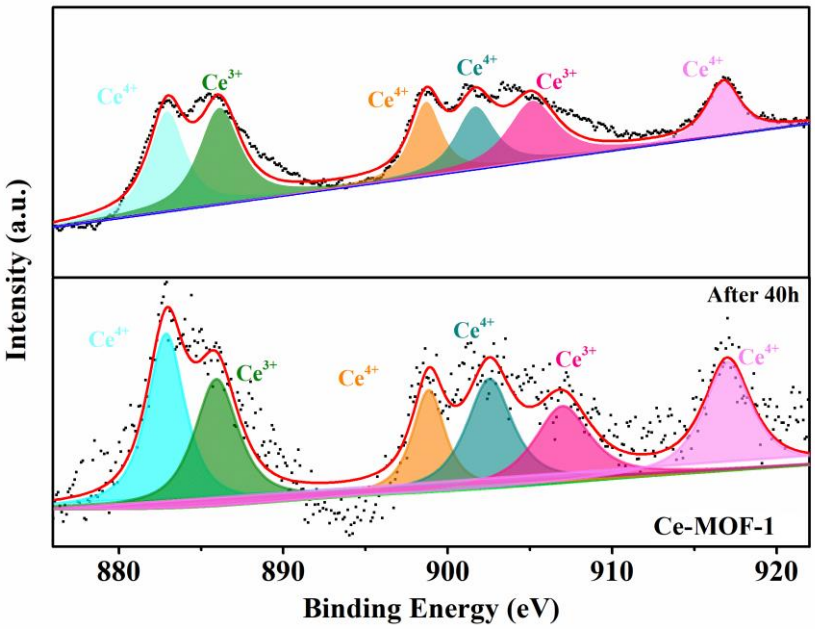

Figure S28. Ce 2p XPS spectra of Ce-MOF-1 after cycles.

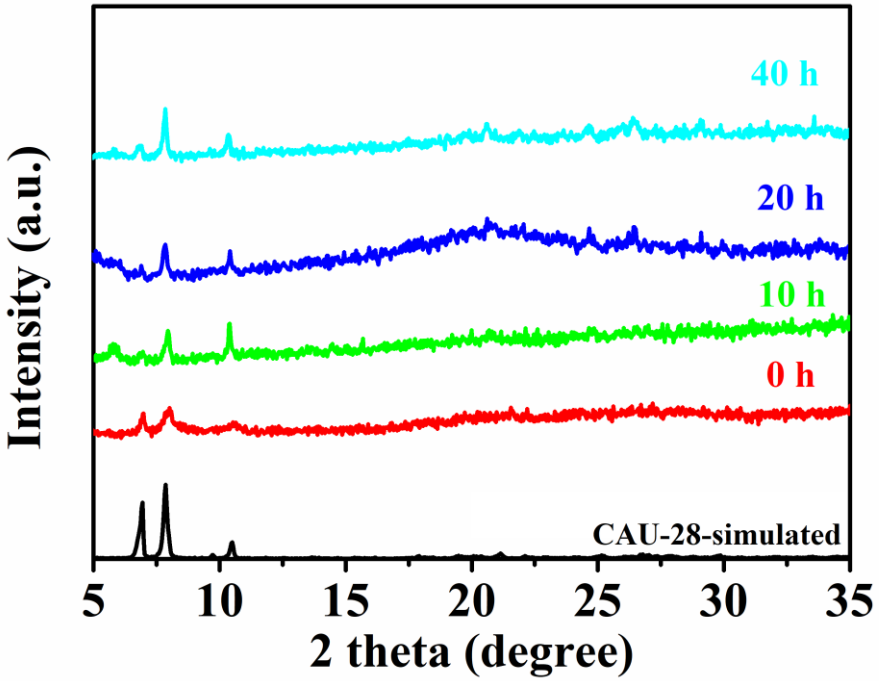

Figure S29. In situ XRD of the symmetric cell with Ce-MOF-1.

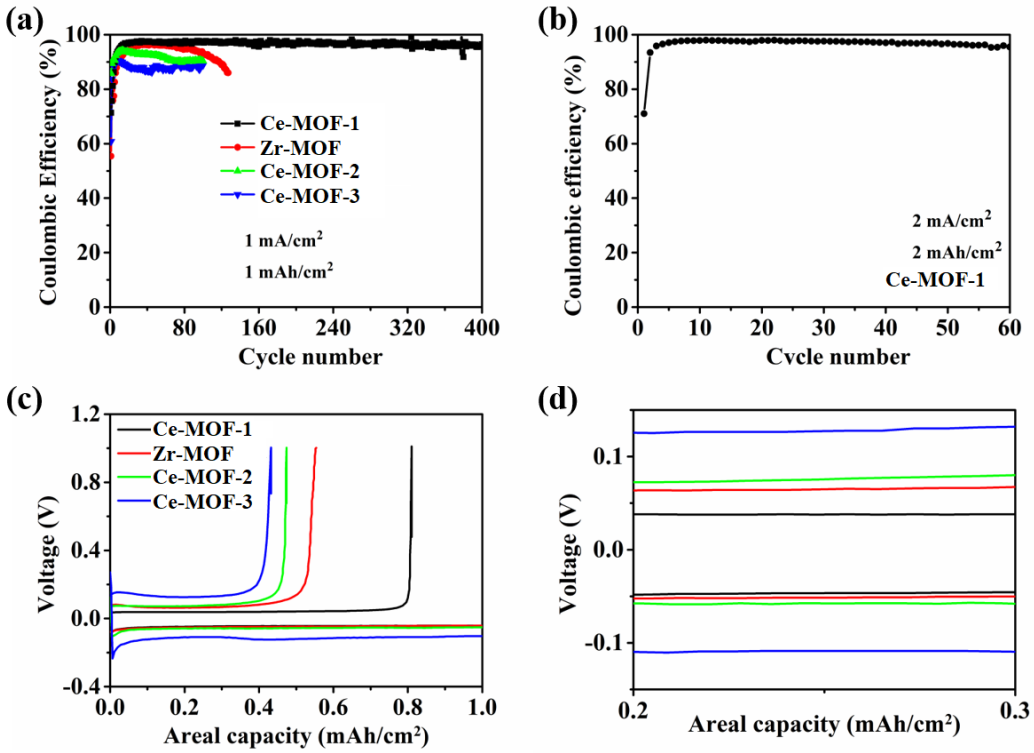

Figure S30. (a) The coulomb efficiency of Li-Cu cell with different separators at an areal capacity of 1 mAh cm^{-2} with the current density of 1 mA cm^{-2}. (b) The coulomb efficiency of Li-Cu cell with Ce-MOF-1 at an areal capacity of 2 mAh cm^{-2} with the current density of 2 mA cm^{-2}. (c) The Voltage curve of the Li|Cu cells with different separators at first cycle. (d) The enlarged pictures of the Voltage curve of the Li|Cu cells with different separators at first cycle.

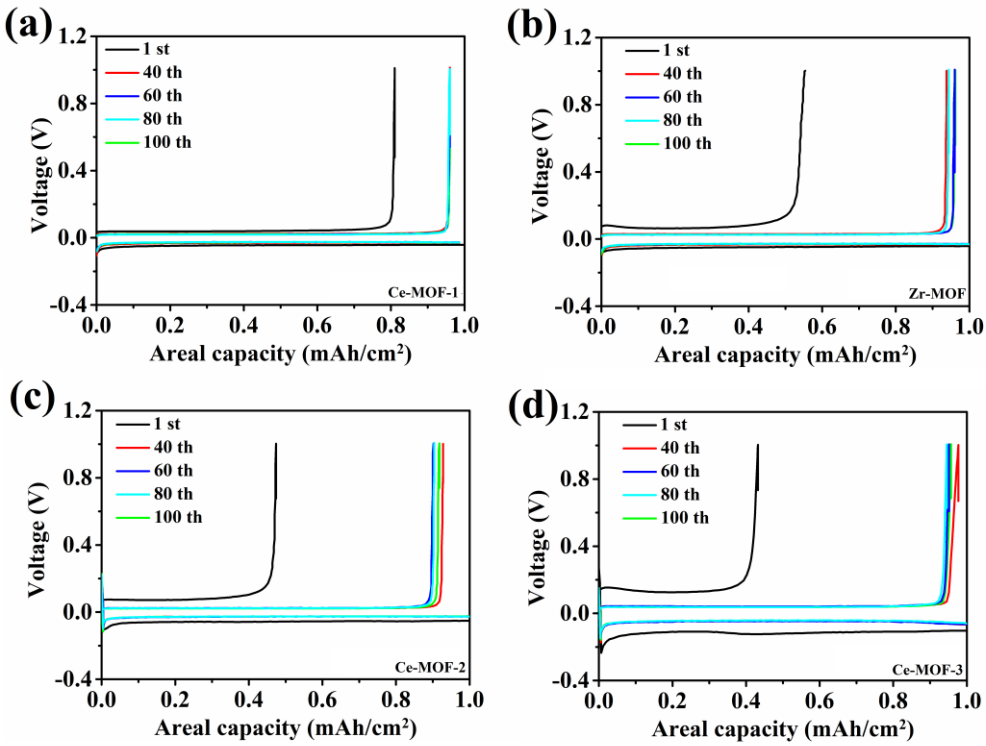

Figure S31. Voltage curves of the Li|Cu cells with different separators at different cycles.

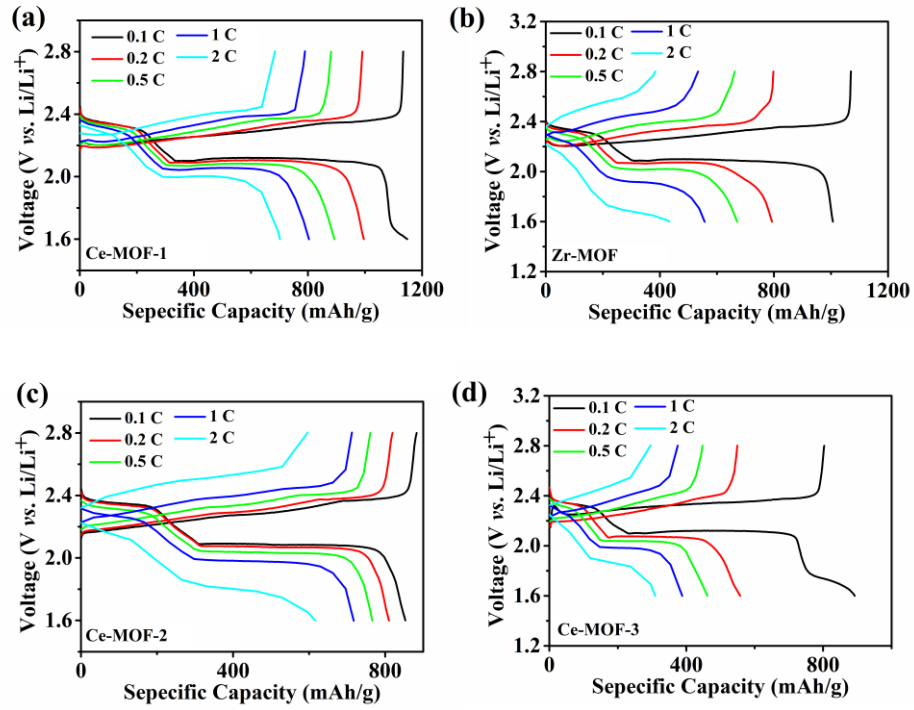

Figure S32. Voltage curves of the Li-S cells with different separators at different current density.

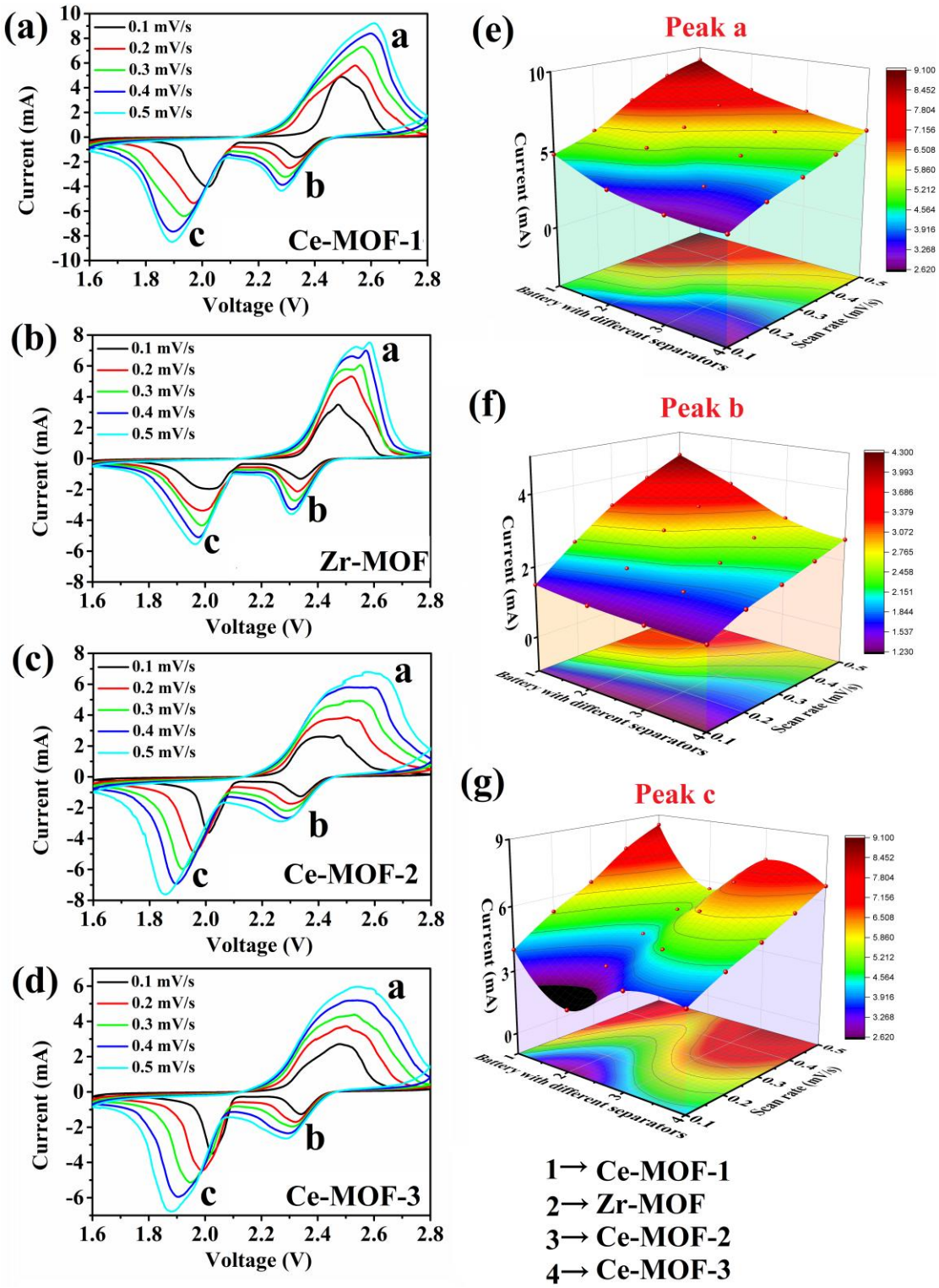

Figure S33. CV curves of the symmetrical cell of (a) Ce-MOF-1, (b) Zr-MOF, (c) Ce-MOF-2 and (d) Ce-MOF-3 under different scanning rate. Corresponding relationship between the scan rate mV/s and current I of different separators for (e) peak a, (f) peak b and (g) peak c.

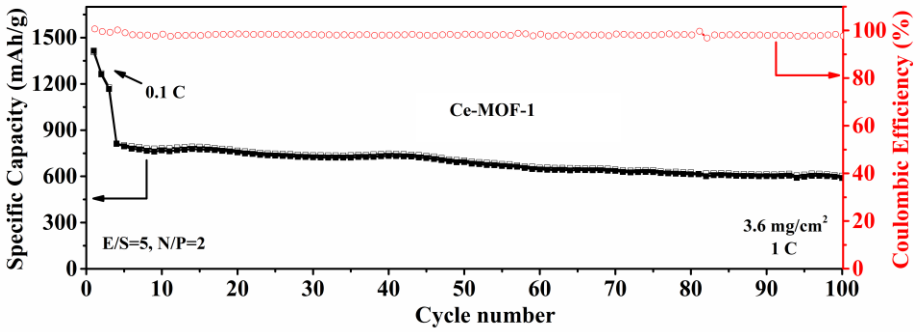

Figure S34. Cycling performance of the Li–S batteries with Ce-MOF-1 at 1 C rate.

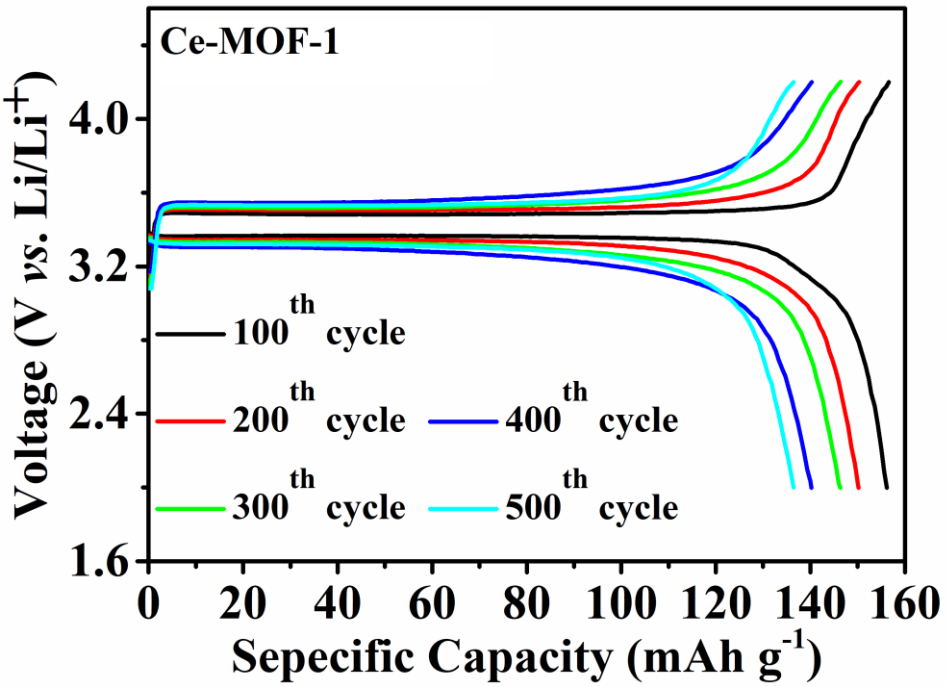

Figure S35. Voltage curves of the Li- LFP cells with Ce-MOF-1 at different cycles.

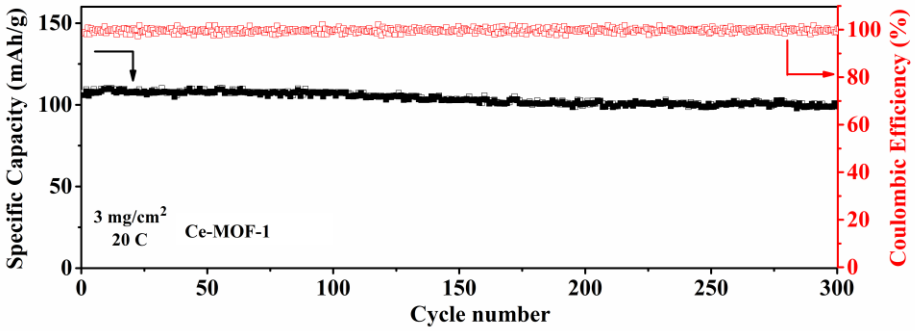

Figure S36. Cycling performance of the Li– LFP batteries with Ce-MOF-1 at 20 C rate.

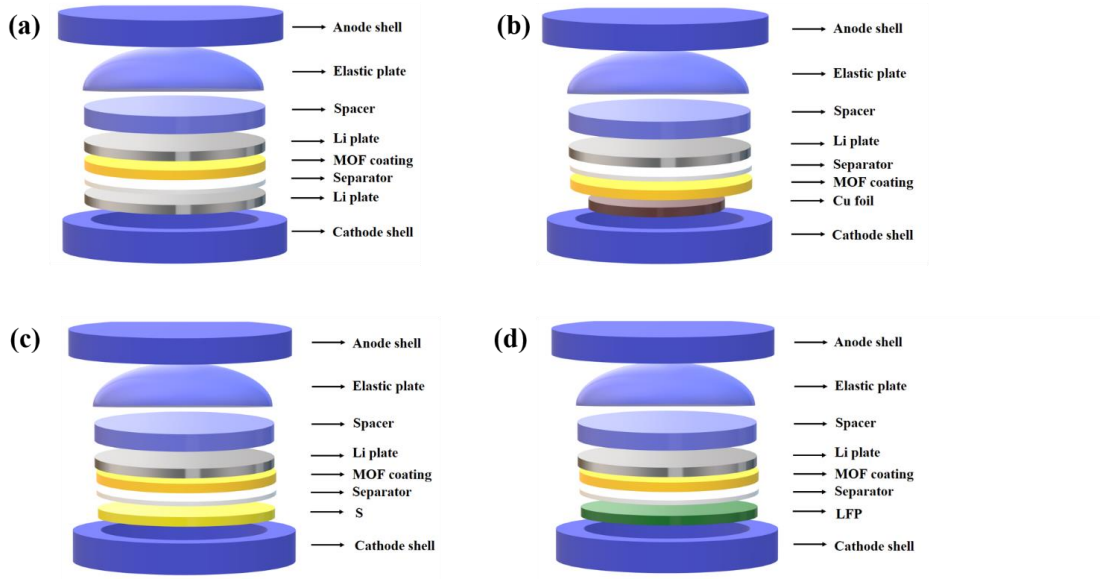

Figure S37. All battery assembly methods that appear in this article.

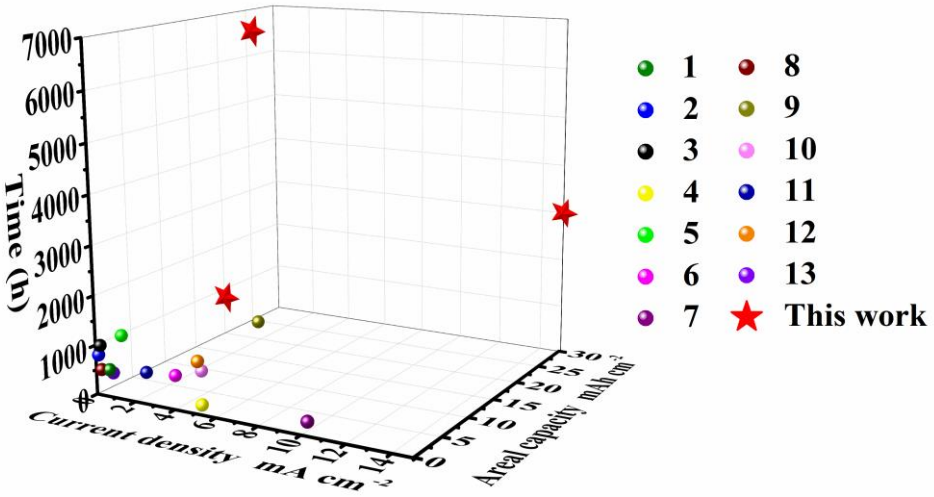

Figure S38 The comparison of Li-Li symmetric cells performance comparison of Ce-MOF-1 with different lithium metal protection.

As shown in **Figure S38**, at 15 mA cm^{-2} and 30 mAh cm^{-2}, the symmetric cell with Ce-MOF-1 ran stably for more than 3000 h, which is far superior to previously reported lithium protection strategies.

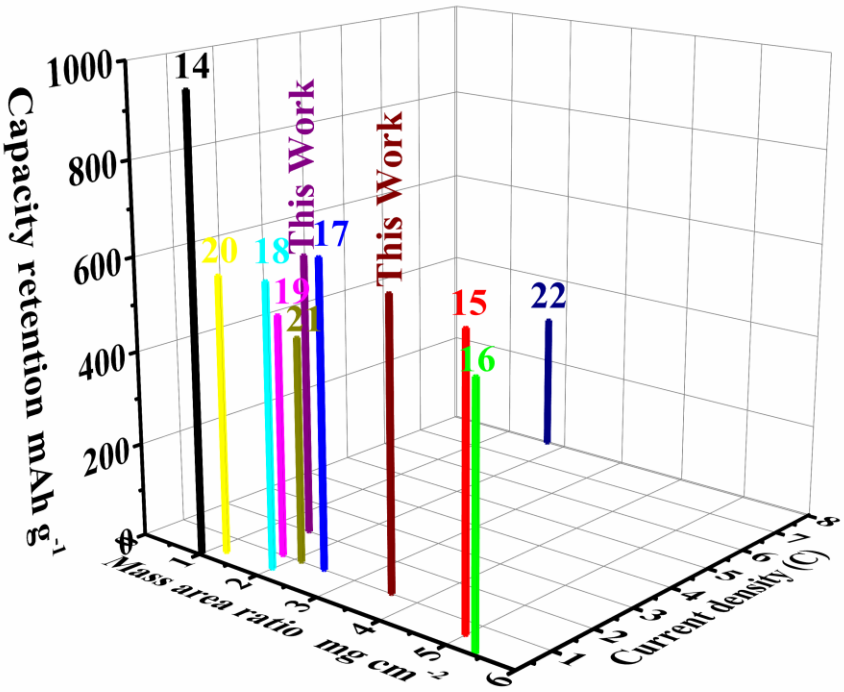

Figure S39. The comparison of the electrochemical performances of the lithium-sulfur cells using different lithium metal protection strategy reported in the literatures.

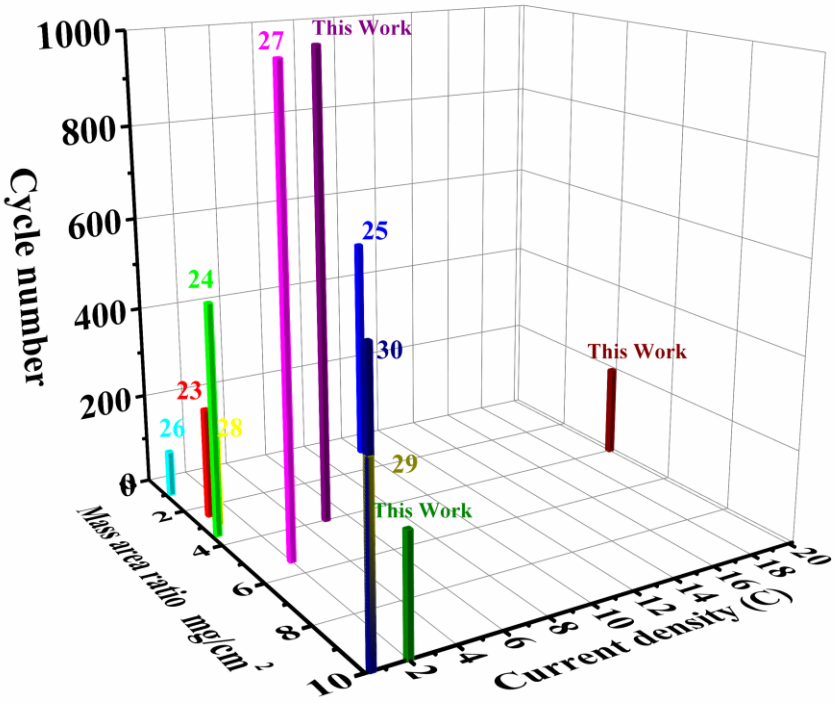

Figure S40. The comparison of the electrochemical performances of the Li-$LiFeO_4$ cells using different lithium metal protection strategy reported in the literatures.

Table S1. The Li-Li symmetric cells performance comparison of Ce-MOF-1 with different lithium metal protection.

Lithium metal protection strategy		**Current density (mA cm^{-2})**	**Cycling capacity (mAh cm^{-2})**	**Cycling time (h)**	**Overpo-tential (mV)**	**Refs.**
Solid electrolyte	PEO-n-UIO electrolytes	0.5	0.5	500	500	1
	ZIF-8	0.1	0.1	800	~50	2
	LATP	0.2	0.1	1000	130.5	3
Lithium interface modification	Li@25ZrEG	5	1	100	250	4
	Li@UCLN	5	1	300	100	5
Lithium deposition carrier	N-doped CNTs/Ni Foam	3	3	400	62	6
	Li–Cu composite anode	10	1	180	400	7
Electrolyte additive	Novel CPE membrane	0.2	0.2	500	70	8
Separator	OVA-PANI-Janus separator	5	10	1200	60	9
	TiO_2-BDC separator	4	4	500	50	10
	UiO-66-NH_2 separator	1.5	3	350	50	11
	UiO-66-SO_3Li separator	5	0.5	1000	42	12
	LP-EMP separator	0.5	1	400	55	13
	Ce-MOF-1 separator	**5**	**10**	**7000**	**78**	**This Work**
		15	**30**	**3000**	**82**	

Table S2. The Li-S performance comparison of Ce-MOF-1 with different materials.

Materials	**Role**	**Mass area ratio (mg cm^{-2})**	**Current density (C)**	**cycles**	**Capacity retention (mAh g^{-1})**	**Ref.**
Z-PMIA separator	Separator	1	0.2	350	961	14
LiSPAN@CuLMA	Cathode	5	0.6	400	~600	15
TpPa-SO_3Li/C elgard separator	Separator	5.4	0.2	100	~535	16
IS-Li	Lithium	2.5	1	500	650	17
A-TiO2-BDC-Coated Separator	Separator	2	0.5	150	~600	18
SnF_2 treated Li	Lithium	1.8	1	1000	511	19
UiO-66-ClO_4 treated Li	Lithium	1.2	0.5	200	587.8	20
LPE-50	Lithium	2.116	1	100	475	21
OCCu-Li	Lithium	1.72	8	400	~300	22
Ce-MOF-1	**Separator**	**1.5**	**2**	**800**	**600.2**	**This Work**
		3.6	**1**	**100**	**612.1**	

Table S3. The Li-$LiFeO_4$ performance comparison of Ce-MOF-1 with different materials.

Materials	**Role**	**Mass area ratio (mg cm^{-2})**	**Current density (C)**	**cycles**	**Capacity retention (mAh g^{-1})**	**Ref.**
Sb-Li	Lithium	2.5-3.0	1	240	125	23
NHCF/CN/ZnO	Lithium	3.5-3.8	0.5	500	144	24
Zn MXene layer	Lithium	1	10	500	100	25
PVA-PANI Janus separators	Separator	1	0.5	100	~135	26
UiO-66-ClO_4 treated Li	Lithium	5.4	2	1000	~125	20
VDF-HFP	gel electrolyte	3	1	200	126	27
PVA-protected Li	Lithium	10	0.5	400	~123	28
NHPM	Lithium	10	0.5	600	116.8	29
Ce-MOF-1	**Separator**	**4**	**5**	**1000**	**124**	**This Work**
		4	**10**	**200**	**116.6**	
		3	**20**	**300**	**100.2**	
		10	**2**	**250**	**132.7**	

References

1 J.-F. Wu, X. Guo, *J. Mater. Chem. A* 2019, **7**, 2653-2659.
2 G. Wang, P. He, L.-Z. Fan, *Adv. Funct. Mater.* 2021, **31**, 2007198.
3 J.-Y. Liang, X.-X. Zeng, X.-D. Zhang, T.-T. Zuo, M. Yan, Y.-X. Yin, J.-L. Shi, X.-W. Wu, Y.-G. Guo, L.-J. Wan, *J. Am. Chem. Soc.* 2019, **141**, 9165-9169.
4 K. R. Adair, C. Zhao, M. N. Banis, Y. Zhao, R. Li, M. Cai, X. Sun, *Angew. Chem., Int. Ed.* 2019, **58**, 15797-15802.
5 W. Guo, Q. Han, J. Jiao, W. Wu, X. Zhu, Z. Chen, Y. Zhao, *Angew. Chem., Int. Ed.* 2021, **60**, 7267-7274.
6 Z. Zhang, J. Wang, X. Yan, S. Zhang, W. Yang, Z. Zhuang, W.-Q. Han, *Energy Storage Mater.* 2020, **29**, 332-340.
7 S. Wu, T. Jiao, S. Yang, B. Liu, W. Zhang, K. Zhang, *J. Mater. Chem. A* 2019, **7**, 5726-5732.
8 J. Yu, Y.-Q. Lyu, J. Liu, M. B. Effat, S. C. T. Kwok, J. Wu, F. Ciucci, *J. Mater. Chem. A* 2019, **7**, 17995-18002.
9 L. Xu, X. Y. Daphne Ma, W. Wang, J. Liu, Z. Wang, X. Lu, *J. Mater. Chem. A* 2021, **9**, 3409-3417.
10 Y. Zhong, F. Lin, M. Wang, Y. Zhang, Q. Ma, J. Lin, Z. Feng, H. Wang, *Adv. Funct. Mater.* 2020, **30**, 1907579.
11 L. Shen, H. B. Wu, F. Liu, C. Zhang, S. Ma, Z. Le, Y. Lu, *Nanoscale Horiz.* 2019, **4**, 705-711.
12 Z. Wang, W. Huang, J. Hua, Y. Wang, H. Yi, W. Zhao, Q. Zhao, H. Jia, B. Fei, F. Pan, *Small Methods* 2020, **4**, 2000082.
13 C. Zhang, L. Shen, J. Shen, F. Liu, G. Chen, R. Tao, S. Ma, Y. Peng, Y. Lu, *Adv. Mater.* 2019, **31**, 1808338.
14 J. Liu, J. Wang, L. Zhu, X. Chen, Q. Ma, L. Wang, X. Wang, W. Yan, *Chem. Eng. J.* 2021, **411**, 128540.
15 Z. Jiang, H.-J. Guo, Z. Zeng, Z. Han, W. Hu, R. Wen, J. Xie, *ACS Nano* 2020, **14**, 13784-13793.
16 Y. Cao, H. Wu, G. Li, C. Liu, L. Cao, Y. Zhang, W. Bao, H. Wang, Y. Yao, S. Liu, F. Pan, Z. Jiang, J. Sun, *Nano Lett.* 2021, **21**, 2997-3006.
17 J. Liu, Y. Cao, J. Zhou, M. Wang, H. Chen, T. Yang, Y. Sun, T. Qian, C. Yan, *ACS Appl. Mater. Interfaces* 2020, **12**, 54537-54544.
18 Y. Zhong, F. Lin, M. Wang, Y. Zhang, Q. Ma, J. Lin, Z. Feng, H. Wang, *Adv. Funct. Mater.* 2020, **30**, 1907579.
19 W. Guo, Q. Han, J. Jiao, W. Wu, X. Zhu, Z. Chen, Y. Zhao, *Angew. Chem., Int. Ed.* 2021, **60**, 7267-7274.
20 G. Jiang, K. Li, F. Yu, X. Li, J. Mao, W. Jiang, F. Sun, B. Dai, Y. Li, *Adv. Energy Mater.* 2021, **11**, 2003496.
21 Y. Wang, C.-F. Lin, J. Rao, K. Gaskell, G. Rubloff, S. B. Lee, *ACS Appl. Mater. Interfaces* 2018, **10**, 24554-24563.
22 X.-Y. Yue, J. Bao, Q.-Q. Qiu, R.-J. Luo, Q.-C. Wang, X.-J. Wu, Y.-N. Zhou, *Chem. Eng. J.* 2020, **391**, 123516.
23 T. Chen, W. Kong, P. Zhao, H. Lin, Y. Hu, R. Chen, W. Yan, Z. Jin, *Chem. Mater.* 2019, **31**, 7565-7573.
24 X.-L. Zhang, Z.-Q. Ruan, Q.-T. He, X.-J. Hong, X. Song, Q.-F. Zheng, J.-H. Nie, Y.-P. Cai, H. Wang, *ACS Appl. Mater. Interfaces* 2021, **13**, 3078-3088.
25 J. Gu, Q. Zhu, Y. Shi, H. Chen, D. Zhang, Z. Du, S. Yang, *ACS Nano* 2020, **14**, 891-898.
26 L. Xu, X. Y. Daphne Ma, W. Wang, J. Liu, Z. Wang, X. Lu, *J. Mater. Chem. A* 2021, **9**, 3409-3417.
27 T. Chen, W. Kong, Z. Zhang, L. Wang, Y. Hu, G. Zhu, R. Chen, L. Ma, W. Yan, Y. Wang, J. Liu, Z. Jin, *Nano Energy* 2018, **54**, 17-25.
28 Y. Zhao, D. Wang, Y. Gao, T. Chen, Q. Huang, D. Wang, *Nano Energy* 2019, **64**, 103893.
29 X. Li, Z. Chu, H. Jiang, Y. Dai, W. Zheng, A. Liu, X. Jiang, G. He, *Energy Storage Mater.* 2021, **37**, 233-242.